Introduction to nonlinear optical spectroscopic techniques for investigating ultrafast processes

Eric Vauthey

Dpt. of physical chemistry, University of Geneva, Switzerland

Eric Vauthey has studied chemistry at the University of Fribourg where he obtained his PhD in 1989 under the supervision of Profs Paul Suppan and Edwin Haselbach. He went then for post-docs to the Royal Institution and to Imperial College in the group of Prof. David Phillips and to the ETH in Zürich in the group of Prof. Urs Wild. In 1992, he came back to Fribourg as a Lecturer and could start his own research. He obtained his habilitation in 1998 and was appointed as full Professor of physical chemistry at the University of Geneva in 2001.

The research of Eric Vauthey and his team is focused on the development and the applications of optical spectroscopic techniques to investigate ultrafast processes in the condensed phase, taking place between a few tens of femtoseconds to a few nanoseconds. These techniques include four-wave mixing, transient absorption, fluorescence up-conversion and time-resolved second harmonic generation. The main interest lies in the understanding of the dynamics of ultrafast processes, such as photoinduced charge transfer, excitation energy transfer, vibrational and solvent relaxation in bulk liquid solutions, at interfaces and in biological and organised environments.

Summary

The aim of this lecture is to introduce the most used nonlinear optical spectroscopic techniques for investigating ultrafast processes in the condensed phase.

The basic concepts of nonlinear optics (nonlinear susceptibility, nonlinear polarisation, frequency mixing, phase matching condition, ...) are first briefly summarized in Section 2. Section 3 is devoted to second-order nonlinear spectroscopies. It will be shown that these techniques are very powerful for investigating processes at surfaces and interfaces. The principles of surface second-harmonic generation (SHG) and sum-frequency generation (SFG) and of their time-resolved variants are discussed, and their applications are illustrated by several examples.

The third order nonlinear susceptibility, $\chi^{(3)}$, as well as the basic theoretical concepts required to understand four wave-mixing processes in isotropic media are introduced in Section 4.

In the next section, third-order nonlinear spectroscopic techniques performed with two beams are discussed. The first one is the transient Kerr effect: it can be considered as a time-domain low frequency Raman spectroscopy and allows the dynamics of liquids to be investigated. The second one is the transient dichroism also called polarisation spectroscopy: it can be used to investigate population dynamics or processes leading to a reorientation of the transition dipole moments of the sample molecules. Optical heterodyne detection, which offers the possibility to measure separately the real and imaginary parts of the nonlinear susceptibility is also presented.

Section 6 is dedicated to the most basic four wave-mixing techniques, i.e. third-order nonlinear spectroscopic methods performed with three different optical beams and where the signal propagates in a distinct direction. These methods are discussed using both the transient grating (or transient holography) and the nonlinear optics formalisms. Applications of these techniques for performing ultrafast calorimetry and for measuring population dynamics, transient dichroism, as well as polarisation selective transient grating are illustrated by several examples.

Advanced four wave-mixing techniques are presented in Section 7. The first one is CARS (Coherent Anti-Stokes Raman Scattering) spectroscopy that is introduced using the grating picture. The various contributions to the signal that influence CARS lineshape are exposed. Applications of electronic resonant CARS and time-resolved CARS are presented. The second advanced method is the photon-echo technique, which is also explained using the grating picture. The concepts of homogeneous and inhomogeneous lineshape are briefly discussed. The origin of a photon echo is first explained for the case of a purely inhomogenously broadened band. Finally, the three-pulse photon echo peak shift technique that allows the distinction between photon echo and free induction decay signals is explained and one of its applications is illustrated by an example.

1. Introduction

The field of nonlinear optical spectroscopy is characterised by a rather large number of experimental techniques very often associated with quite cryptic acronyms such as TG-OKE, CARS or 3PEPS, to name a few of them. To a non-specialist, this may give the impression of a high complexity and of a huge variety of non-linear optical spectroscopies. Actually this is not really true as several nonlinear spectroscopies with different names are in fact very similar and sometimes even identical. For example, the widely used transient absorption spectroscopy could in principle also be called 'time-domain multiplexed two-beam heterodyne four-wave mixing spectroscopy'. One reason for the existence of all these different names and acronym is that nonlinear optical spectroscopy involves several interactions between the optical field and matter. As each optical field is characterised by many parameters, such as frequency, polarisation, arrival time, wavevector, ..., the larger the number of interactions the larger the number of different combinations of optical field parameters, hence of possible experiments.

The aim of this lecture is not to review all the non-linear optical spectroscopies that have been developed over the past decades but to give a basic introduction to the most important experimental concepts that underlie them. There are essentially two reasons to perform nonlinear optical spectroscopy: 1) to measure sample properties that cannot be addressed by 'conventional' linear optical spectroscopy or 2) to obtained spectroscopic information with a higher resolution or sensitivity than that associated with linear spectroscopy.

Our research group is essentially involved in the investigation of ultrafast photophysical and photochemical processes in liquids. Therefore this lecture will mainly focussed on the nonlinear optical techniques that we are familiar with and that yield new insight into the dynamics of photoinduced processes in liquid solutions or at liquid interfaces.

The very basic concepts of nonlinear optics will be first briefly discussed. Then, various nonlinear optical spectroscopic methods will be described. We will start with techniques involving second-order interactions and continue with methods based on third-order nonlinear interactions.

2. Basic concepts of nonlinear optics

An electric field applied on a dielectric material induces a macroscopic electric dipole moment called *polarisation*, $\mathbf{P}(\omega)$[1]. The induced polarisation exhibits a linear dependence on the electric field, $\mathbf{E}(\omega)$:

$$\mathbf{P}(\omega) = \boldsymbol{\chi}(\omega)\cdot\mathbf{E}(\omega) \tag{1}$$

where $\boldsymbol{\chi}(\omega)$ is the optical susceptibility of the material and ω the angular frequency.

The optical susceptibility is usually expressed in terms of the complex refractive index, $\tilde{\mathbf{n}}$:

$$\tilde{\mathbf{n}}(\omega) = \left(1 + \boldsymbol{\chi}(\omega)\right)^{1/2} \tag{2}$$

---

[1] Bold symbols denote vectors or tensors. A list of symbols can be found at the end of this document (Section 9).

ñ as well as **χ** are in principle second rank tensors but, as we are interested in the liquid phase, we will consider only it orientationally-averaged value, $\tilde{n} = Tr(\tilde{\mathbf{n}})/3$. The latter is usually split into real and imaginary parts:

$$\tilde{n} = n + iK \tag{3}$$

where n is the refractive index and K is the attenuation constant, which is directly connected with the absorbance of the material, A :

$$K = \frac{\ln 10 \; A\lambda}{4\pi L} \tag{4}$$

where L is the optical pathlength and λ the wavelength. K and n are related by the Kramers-Kronig relationship :

$$n(\omega) = -\frac{1}{\pi} \int \frac{K(\omega')}{(\omega - \omega')} d\omega' \tag{5}$$

The polarisation, **P**(ω), acts as a source of radiation at the frequency ω. In principle, all the optical properties of a material and the corresponding phenomena (absorption, refraction, reflection, diffusion, ...) are associated with **P**(ω) as defined in eq.(1). In those processes the polarisation oscillates at the same frequency as the incoming electric field.

When the electric field of the light is intense, **χ** itself depends on the electric field and thus the polarisation can be expressed in a power series of **E** [1,2]:

$$\mathbf{P} = \mathbf{P}^L + \mathbf{P}^{NL} = \varepsilon_0 \left[\boldsymbol{\chi}^{(1)} \cdot \mathbf{E} + \boldsymbol{\chi}^{(2)} \cdot \mathbf{E} \cdot \mathbf{E} + \boldsymbol{\chi}^{(3)} \cdot \mathbf{E} \cdot \mathbf{E} \cdot \mathbf{E} \right] \tag{6}$$

where **χ**$^{(1)}$ is the linear optical susceptibility and corresponds to the susceptibility at low intensity. **χ**$^{(2)}$ is the second-order nonlinear optical susceptibility and is a third rank tensor containing 27 elements, which correspond to the possible combinations of the three Cartesian components of the polarisation and of the two interacting electric fields. **χ**$^{(3)}$ is the third-order nonlinear optical susceptibility and is a fourth rank tensor with 3^4 elements.

The order of magnitude of the elements of **χ**$^{(1)}$ is 1, that of the elements of **χ**$^{(2)}$ is 10^{-12} m/V and that of **χ**$^{(3)}$ is 10^{-23} m^2/V^2. Therefore, a nonlinear relationship between the polarisation and the electric field appears only with strong fields.

The relationship between the light intensity I and the electric field amplitude is:

$$I = 2n \left(\frac{\varepsilon_0}{\mu_0} \right)^{1/2} \left| \vec{E}_0 \right|^2 \tag{7}$$

where μ_0 and ε_0 are the vacuum permeability and permittivity, respectively

Some numerical examples are illustrated in Table 1.

Table 1: Electric field associated with various light intensity.

I (W/cm^2)	1	10^3	10^6	10^9	10^{12}
E_0 (V/m)	$1.37 \cdot 10^3$	$4.34 \cdot 10^4$	$1.37 \cdot 10^6$	$4.34 \cdot 10^7$	$1.37 \cdot 10^9$

Such high intensities can be easily realised by focusing laser pulses. For example, the light intensity in a 10 ns, 1 mJ pulse focused to a spot of 10 μm diameter amounts to 0.3 GW/cm^2. With pulses of 100 fs duration, this intensity is reached with an energy of 10 nJ/pulse.

These intense optical pulses are associated with electric fields that start to scale with those existing between the charges, nuclei and electrons, constituting matter. Therefore, the optical properties of the material are modified.

Let us consider the second-order polarisation in a material with a second-order nonlinear susceptibility irradiated with an optical field oscillating at two frequencies, ω_1 and ω_2:

$$P_i^{(2)} = \varepsilon_0 \chi_{ijk}^{(2)} \cdot E_j(\omega_1, \omega_2) \cdot E_k(\omega_1, \omega_2) \qquad (8)$$

where the indices i, j and k denote the Cartesian components of the polarisation and of the incoming fields, respectively, and $\chi_{ijk}^{(2)}$ is the relevant tensor element of the second-order nonlinear susceptibility, $\chi^{(2)}$. From this equation, it appears that the nonlinear polarisation does not oscillate at ω_1 and ω_2 but rather at new frequencies: $2\omega_1$, $2\omega_2$, $\omega_1+\omega_2$, $|\omega_1-\omega_2|$, and even at $\omega=0$. This nonlinear polarisation acts as a source of radiation at those new frequencies. This is at the origin of well-known nonlinear phenomena such as second harmonic generation (SHG), sum frequency generation (SFG), difference frequency mixing (DFM), and optical rectification (OR). In OR, the generated field is not constant but follows the envelope of the incoming pulses.

The intensity, I_i, of the field generated by the polarisation at a given frequency, ω_3, is:

$$I_i(\omega_3) \propto \left| \chi_{ijk}^{(2)} \right|^2 I_j I_k L^2 \cdot \mathrm{sinc}^2\left(\frac{\Delta k L}{2} \right) \qquad (9)$$

with $\mathrm{sinc}(x) = \sin(x)/x$. L is the optical pathlength and Δk is the so-called wavevector (or phase) mismatch:

$$\Delta k = \mathbf{k}_{out} - \sum \mathbf{k}_{in} \qquad (10)$$

where $\mathbf{k}_{out}$ is the wavevector of the new outgoing field and $\mathbf{k}_{in}$ are the wavevectors of the incoming fields ($|\mathbf{k}|=k=n\omega/c$). The new field intensity is the largest when $\Delta k=0$. This corresponds to momentum conservation, as momentum is $\mathbf{p} = \hbar\mathbf{k}$. For example for SFG, $\omega_3=\omega_1+\omega_2$ and momentum conservation (or phase-matching condition), $\Delta k=0$, imposes that $\mathbf{k}_3=\mathbf{k}_1+\mathbf{k}_2$. If this condition is not fulfilled, the fields generated at the different locations along the optical pathlength in the material interfere destructively with each other and no efficient frequency conversion is achieved. An important consequence is that SHG, SFG and DFM cannot be realised simultaneously as their respective phase-matching conditions are different. For example, the phase-matching condition for DFM ($\omega_3=\omega_1-\omega_2$; $\omega_1 > \omega_2$) is $\mathbf{k}_3=\mathbf{k}_1-\mathbf{k}_2$.

3) Second-order nonlinear optical spectroscopies

There are essentially two main applications of nonlinear spectroscopic methods:
1) Determination of the second-order nonlinear susceptibility of materials;
2) Investigation of interfacial processes.

The reason for this rather limited number of applications is quite simple: the second order nonlinear susceptibility of centrosymmetric material is zero. This implies that molecules with a centre of inversion have no second-order nonlinear susceptibility. The same applies to isotropic materials such as liquids, glasses or polymers where the constituting molecules (even non-centrosymmetric) have a random orientation. This can be demonstrated in many different ways. The simplest is to consider the even order polarisations:

$$P^{(2n)} = \chi^{(2n)} E^{2n} \qquad\qquad (n = 1, 2, 3, ...)$$

In a centrosymmetric medium, the sign of $P^{(2n)}$ is reversed if the direction of the electric field is reversed:

$$-P^{(2n)} = \chi^{(2n)}(-E)^{2n}$$
$$-P^{(2n)} = \chi^{(2n)} E^{2n}$$

therefore $-P^{(2n)} = P^{(2n)}$, which is only possible if $\chi^{(2n)} = 0$.

Consequently, only non-centrosymmetric materials exhibit even order nonlinear optical properties. Isotropic materials like liquids show only odd order nonlinear effects.
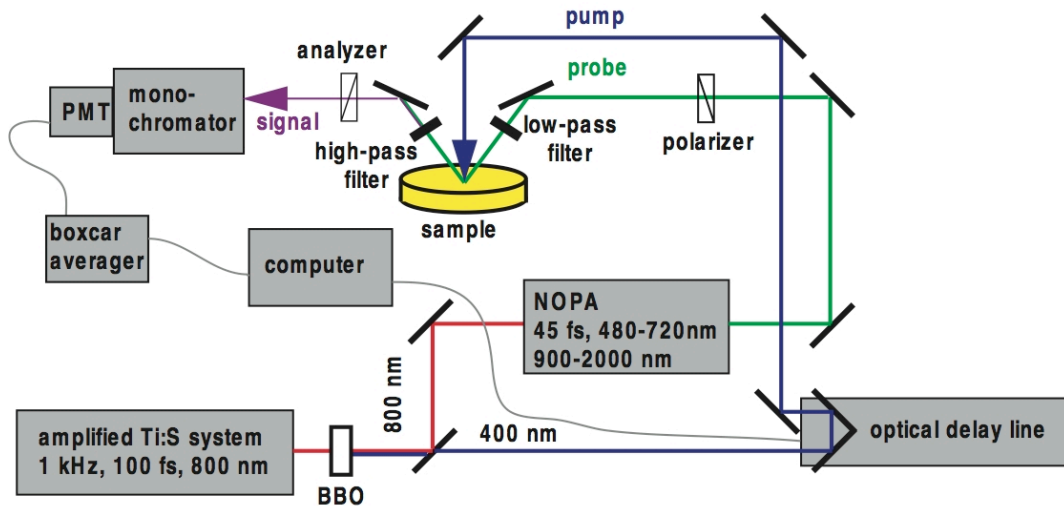
Figure 1: Experimental setup for time-resolved surface SHG. A SHG spectrum can be obtained by blocking the pump pulse and tuning the probe wavelength. The low-pass filter eliminates SHG light generated at the surface of the various optical elements.

The absence of second-order nonlinear response of centrosymmetric materials can be advantageously used to study selectively the interface between two isotropic materials [3-5]. Indeed, such an interface is no longer centrosymmetric and therefore has a non-vanishing second-order nonlinear response. The interface has a $C_{\infty v}$ symmetry that can be reduced to C_{4v} and thus $\chi^{(2)}$ posses 5 non-zero tensor elements.

As a consequence, second-order nonlinear phenomena such as SHG and SFG can take place at an interface. If one irradiates the surface of an isotropic liquid in contact with air with a beam at ω_1 and detects a signal at $2\omega_1$, one can be sure that this signal originates exclusively from the air/liquid interface. This is a very valuable feature as interfaces are extremely difficult to access spectroscopically. Indeed if one performs conventional spectroscopy by irradiating the interfacial region between two bulk media, the signal arising from the interface is totally buried in that originating from the bulk phases.

A typical experimental arrangement for SHG at air/liquid interfaces is illustrated in Figure 1. In principle, both the transmitted and reflected SHG signal can be recorded. However for practical reasons, one measures in most cases the intensity of the reflected signal. If the SHG is generated with a single beam at ω_1, the reflected SHG signal at $\omega_2=2\omega_1$ is collinear with the reflected ω_1 beam. The SHG signal has to be isolated using a combination of filters and monochromator. On the other hand, surface SFG is performed with two different beams at ω_1 and ω_2, and the direction of propagation of the reflected SFG signal at ω_3 is calculated according to the following relationship:

$$\omega_1 \sin\theta_1 + \omega_2 \sin\theta_2 = \omega_3 \sin\theta_3 \qquad (11)$$

where the angles are defined in Figure 2. Equation (11) corresponds to the conservation of photon momentum at the interfacial plane. The signal intensity is:

$$I_S(\omega_3) \propto \left| f_{ijk} \chi_{ijk}^{(2)} \right|^2 I(\omega_1) I(\omega_2) \qquad (12)$$

where f_{ijk} is the nonlinear Fresnel factor for the signal field, which is the nonlinear equivalent of the Fresnel factor for transmission and reflection at an interface between media of different refractive indices. For example, the SFG and SHG signal intensity is in general much larger at liquid-liquid or liquid-solid interface than at air/liquid interface. Indeed, the nonlinear Fresnel factors are the largest when the angle of incidence of the incoming field in the high refractive index medium is around the critical angle for total internal reflection.
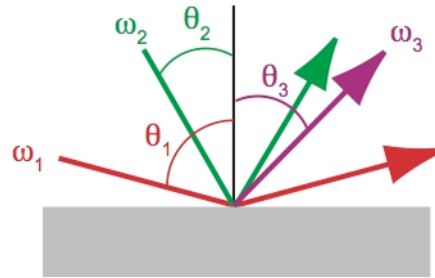

Figure 2: Beam arrangement for SFG at an air-liquid interface.

Like the linear susceptibility, $\chi^{(2)}$ is frequency dependent. A detail discussion of the frequency dependence of nonlinear susceptibility is rather lengthy and goes beyond the scope of this lecture [1,2]. It is sufficient to realise that $\chi^{(2)}$ becomes very large near 'so-called' resonances, i.e. when the frequency of the fields involved in the process coincides with that of a transition between two energy levels of the material. Resonances for SHG and SFG are illustrated in Figure 3.

An important consequence of resonance is that the transition frequencies between two energy levels of a system can be obtained from the frequency dependence of $\chi^{(2)}$. In practice, one measures the intensity of the SFG (or SHG) signal while tuning ω_1 (or ω_2). The so-obtained spectrum exhibits bands, which are located at the same frequency as in a conventional absorption spectrum. Additional bands due to two-photon transitions are also visible.

This approach is intensively used to perform vibrational spectroscopy at interfaces [5]. In this case, ω_1 is in the IR region, while ω_2 is in the visible. The SFG intensity in the visible at ω_3 is recorded as a function of ω_1. The resulting spectrum contains similar information as an IR spectrum but is associated with the interfacial region. A major difference from an IR spectrum

is that a vibrational transition is only visible in the SFG signal if it is both IR and Raman active. Thus centrosymmetric molecules cannot be investigated with this technique.
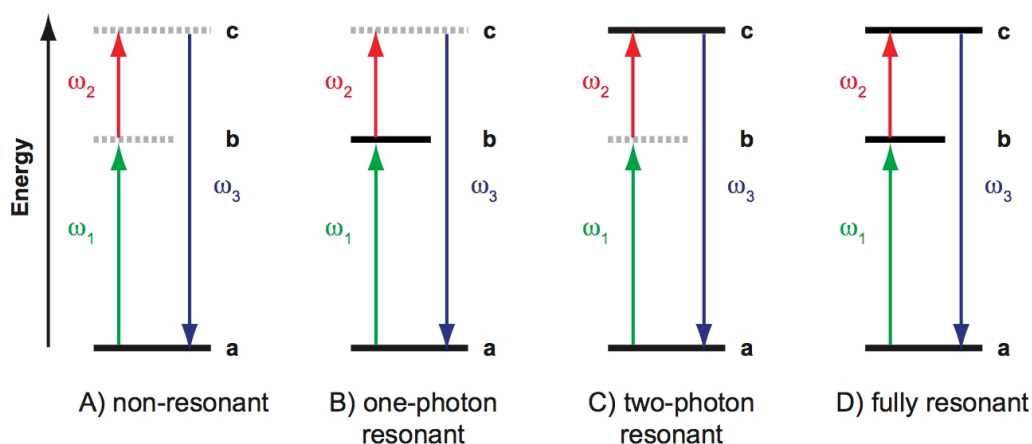
Figure 3: Energy level scheme illustrating the possible resonances in SFG. Solid horizontal lines represent stationary states and dotted lines virtual states.

Similarly surface SHG spectroscopy is performed by recording the SHG intensity as a function of ω_1 [3,4]. The resulting spectrum reflects the linear absorption spectrum of the interfacial region. This approach is mostly used to investigate dye molecules adsorbed at liquid interfaces. As the resonances of the solvents are in general in the far UV, the SHG signal arises essentially from the adsorbed dye molecules when the resonance condition is fulfilled. Here again no resonance enhancement takes place with centrosymmetric molecules. This is easily understood by considering that the second-order nonlinear susceptibility is proportional to the product of the three transition dipole moment involved in SHG, namely $\mu_{ba}\mu_{cb}\mu_{ac}$ (Figure 3). In a centrosymmetric molecule, the wavefunctions of the states have either *g* (gerade) or *u* (ungerade) symmetry and *g-g* as well as *u-u* transitions are forbidden. Thus if state **a** is *u*, states **b** and **c** have to be *g* and *u*, respectively, for μ_{ba} and μ_{cb} to be nonzero. In this case however, μ_{ac} is zero because both **a** and **c** have *u* symmetry.
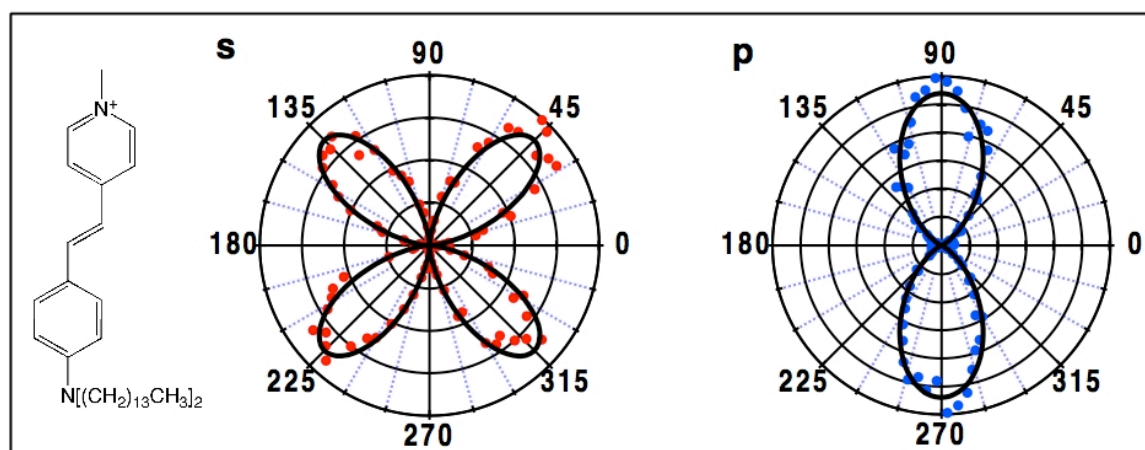

Figure 4: Polar plots representing the intensity of the perpendicular (s) and parallel (p) components of the SHG signal as a function of the polarisation of the incident beam recorded with the dye DiA (left) adsorbed at an air-water interface.

Additionally to the absorption spectrum, information on the orientation of the adsorbed molecules relative to the interface can be obtained by probing the different tensor elements of $\chi^{(2)}$. This is done by measuring the intensity of the signal components polarised parallel and

perpendicular to the plane of incidence as a function of the angle of polarisation of the incident beam relative to the plane of incidence. An example of the output of such measurements is illustrated in Figure 4.

Dynamic information on molecules adsorbed at interfaces can be obtained by performing time-resolved surface SHG (or SFG) [4]. The SHG intensity is measured as a function of the time after excitation of the molecules using the pump-probe technique. A result of such measurements is illustrated in Figure 5. The time profile in A was obtained with malachite green (MG) at an air/water interface after S_0-S_1 excitation at 600 nm (Figure 5B). Probing was performed with pulses at 800 nm and the SHG signal intensity at 400 nm was recorded. In this case, the signal at 400 nm was resonant with the S_0-S_2 transition of MG similarly to the case shown in Figure 3C. The signal intensity is thus proportional to the ground-state (S_0) population of MG. One can see that at time zero, i.e. when the pump pulse excites MG, the SHG signal decreases considerably because ground-state population is depleted. The increase of the SHG signal at t>0 reflects the recovery of the ground-state population from the S_1 state. For MG, this process occurs non-radiatively through a large amplitude motion of the phenyl rings about the single bond to the central carbon atom. The rate of this process depends strongly on the local viscosity and thus such SHG measurements allow interfacial viscosity to be estimated.
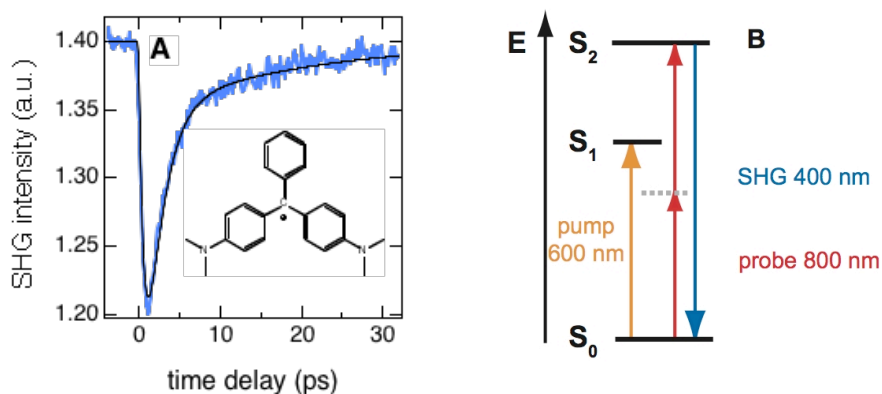
Figure 5: Temporal evolution of the SHG intensity obtained with MG at an air-water interface upon 600 nm excitation (A), and energy level scheme of MG (B).

Although surface SHG and SFG can be performed using nanosecond pulses, one prefers generally femtosecond pulses. In this way, a measurable signal intensity is obtained without too energetic pulses. Surface SHG and SFG are not limited to air-liquid and liquid-liquid interfaces but can also be used to investigate gas (or vacuum)-solid or liquid-solid interfaces or even solid-solid interface. Finally SHG-microscopy allows interfaces in living tissues to be imaged [6].

4) Third-order nonlinear susceptibility

The third-order nonlinear optical susceptibility is the lowest nonlinear order for centrosymmetric materials, i.e. all materials have a third-order nonlinear response. In the following, we will only consider isotropic phases like pure liquid or liquid solutions with randomly oriented solute molecules.

Among the 81 tensor elements of $\chi^{(3)}$, 21 are non zero in such isotropic media. These tensor elements can be classified into four types, which are related as follows [1]:

$$\chi_{1111}^{(3)} = \chi_{1122}^{(3)} + \chi_{1212}^{(3)} + \chi_{1221}^{(3)} \tag{13}$$

The 17 remaining elements can be obtained by permutation of the indices (for example: $\chi_{1122}^{(3)} = \chi_{1133}^{(3)} = \chi_{2211}^{(3)} = \chi_{2233}^{(3)} = \chi_{3311}^{(3)} = \chi_{3322}^{(3)}$). In general, the third-order nonlinear polarisation is given by:

$$P_i^{(3)}(\omega_4) = \varepsilon_0 \chi_{ijkl}^{(3)} E_j(\omega_3) E_k(\omega_2) E_l(\omega_1) \tag{14}$$

If for example, the three incoming fields are polarized along the x axis, the nonlinear response is due to $\chi_{1111}^{(3)}$ and thus the third-order nonlinear polarisation will have a x component only, the tensor elements $\chi_{2111}^{(3)}$ and $\chi_{3111}^{(3)}$ being both zero.

The nonlinear polarisation acts as a source of radiation, whose intensity is given by:

$$I_i(\omega_4) \propto \left| \chi_{ijkl}^{(3)} \right|^2 I_j I_k I_l L^2 \cdot \mathrm{sinc}^2\left(\frac{\Delta kL}{2}\right) \tag{15}$$

In this case as well, the polarisation gives rise to a signal field with a significant intensity only if the phase-matching condition, $\Delta k = 0$, is fulfilled. The frequency ω_4 of the signal depends on those of the three incoming field and on the geometry of the experiment.

For example, if one considers a radiation field containing three frequencies, ω_1, ω_2 and ω_3, interacting with a material, one can see that the third-order polarisation, $P^{(3)}$, contains the following combination of frequencies :

$$\begin{aligned}
&\omega_1 + \omega_2 + \omega_3 \\
&3\omega_n, \; \omega_n \quad n = 1,2,3 \\
&2\omega_m + \omega_n, \; 2\omega_m - \omega_n, \; \omega_m - 2\omega_n \quad m = 1,2,3 \; n \neq m \\
&\omega_m + \omega_n - \omega_p, \; \omega_m - \omega_n - \omega_p \quad n = 1,2,3 \; m \neq n \neq p
\end{aligned}$$

A beam at a given frequency is of course only generated if the phase-matching condition is satisfied. In an isotropic material, this condition cannot be fulfilled for processes where the signal is at the sum frequency of the three applied fields (for example, $\omega_1 + \omega_2 + \omega_3$, $3\omega_n$ and $2\omega_m + \omega_n$). Let's illustrate this with $\omega_4 = 3\omega_1$, where the phase-matching condition is:

$$\mathbf{k_4} = \mathbf{k_1} + \mathbf{k_1'} + \mathbf{k_1''} \tag{16}$$

If the three incoming beams at ω_1 are collinear, the vector notation can be dropped and:

$$k_4 = 3k_1$$

which can be rewritten as:

$$n_4 \frac{\omega_4}{c} = 3n_1 \frac{\omega_1}{c}$$

where n_1 and n_4 represent the refractive index at ω_1 and ω_4, respectively.

As $\omega_4 = 3\omega_1$, the phase-matching condition is fulfilled if: $n_4 = n_1$.

This condition cannot be fulfilled in the isotropic condensed phase as in general $n_4 > n_1$. The wavevector diagram in Figure 6 shows that $\Delta\mathbf{k} = 0$ can never be realised independently on the beam geometry. However, third harmonic generation can be realised in birefringent materials, where the optical fields at ω_4 and ω_1 oscillate along different directions.
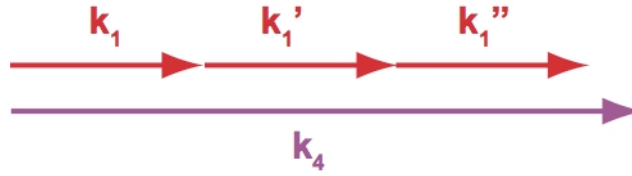
Figure 6: Wavevector diagram for third-harmonic generation in an isotropic dispersive medium.

For the other processes, the phase-matching condition can be satisfied by adjusting the angle of incidence of the various beams, as it will shown below.

5) Third-order nonlinear spectroscopy with two beams: transient Kerr effect and transient dichroism

Third-order nonlinear spectroscopy involves the interaction of three electric fields in the material. However, this does not imply that one absolutely has to use three different laser beams. For example, as will be discussed in more detail in the next section, conventional transient absorption spectroscopy is a third-order nonlinear spectroscopy performed with two beams. We will discuss here third-order nonlinear techniques that are usually performed with two laser beams: the transient optical Kerr effect and the transient dichroism (also called polarisation spectroscopy).

5.1) Transient optical Kerr effect

The optical Kerr effect is an optically induced birefringence that is due to the nonlinear refractive index of the material. At high intensity, the refractive index can be written as:

$$n = n_0 + 2\bar{n}_2 |E_0|^2 \qquad (17)$$

where E is the electric field amplitude, n_0 is the linear refractive index and $\bar{n}_2$ is the second-order nonlinear refractive index. The *second-order* nonlinear refractive index is related to the *third-order* nonlinear susceptibility.

This nonlinear refractive index is easily understood if one considers that the propagation of an intense light beam in a material is accompanied by the orientation of the electric charges along the electric field. The polarisation of the electrons is quasi-instantaneous and follows the oscillations of the electric field even at optical frequencies. If the molecules have a permanent or an induced dipole moment, they reorient along the field. This motion is too slow relatively to the oscillation of the optical field. There are however, components of the field at $\omega = 0$ (OR see section 3), that are slow enough to induce molecular reorientation. After electronic and nuclear reorientation, the material is no longer isotropic and therefore the refractive index along the optical electric field is not the same as that in the other directions. This difference increases with $|E_0|$, i.e. with the light intensity I. This photoinduced birefringence is the *Optical Kerr Effect* (OKE).

Once the electric field is interrupted, the electronic birefringence ceases 'immediately', while the decay of the nuclear birefringence requires molecular reorientation. Consequently, the measurement of the temporal variation of the nuclear birefringence is used to get information on the dynamics of liquids.
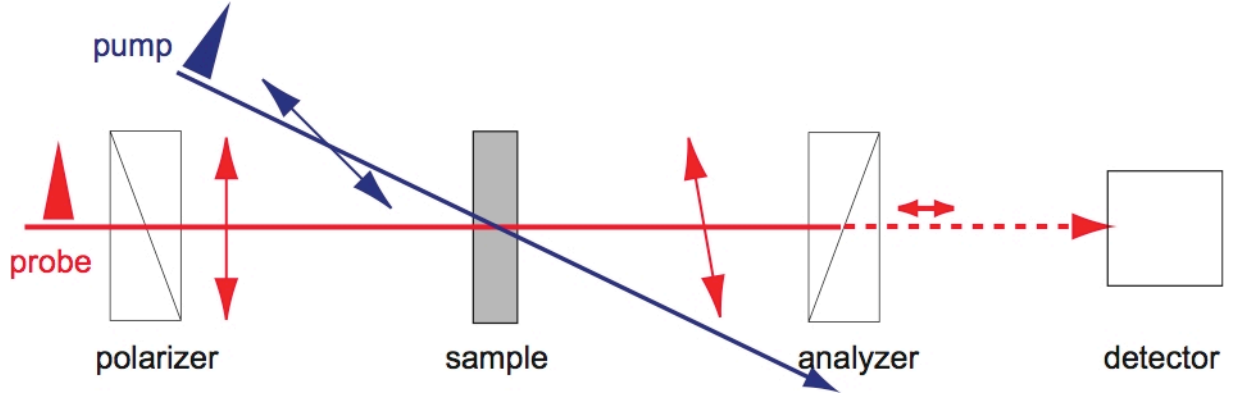
Figure 7: Schematic experimental arrangement for transient OKE.

An experimental setup for measuring OKE dynamics is shown in Figure 7. The sample is located between two crossed polarizers. Therefore, the probe light intensity on the detector is zero, because it is polarised perpendicular to the analyzer. At time $t=0$, the sample is illuminated with a pump pulse linearly polarised at 45^0 relatively to the first polarizer (Figure 8). This pump pulse creates a birefringence through the OKE, the refractive index parallel to the polarisation of the pump field, $n_{\parallel}$, being larger than that perpendicular, $n_{\perp}$.

A

B
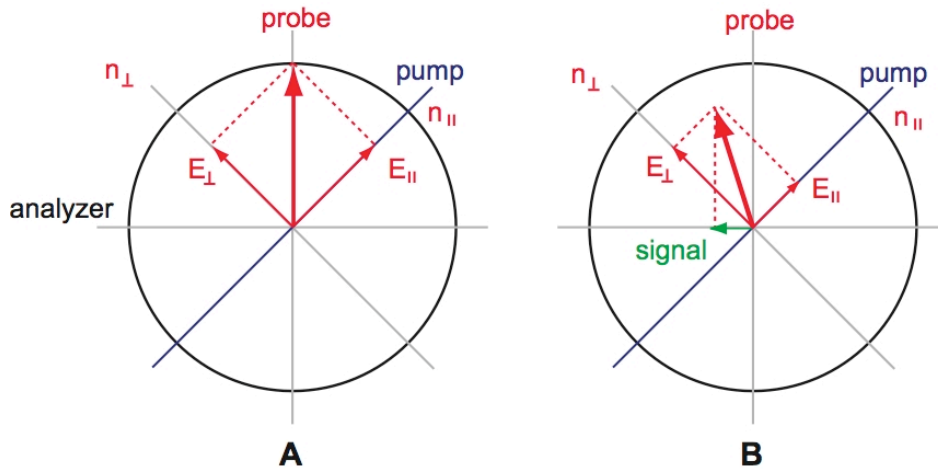
Figure 8: Principles of the OKE measurement: if there is no birefringence (A), the probe pulse is blocked by the analyzer. With birefringence (B), the polarisation of the probe pulse is slightly rotated and its component parallel to the analyzer can cross it.

The electric field associated with the probe pulse can be decomposed into components parallel, $E_{\parallel}$, and perpendicular, $E_{\perp}$, to the polarisation of the pump pulse. At the entrance of the sample, these two components are in phase, $\Delta\phi=0$ (Figure 8A). In the birefringent sample, each component experiences a different refractive index ($n_{\parallel}$ or $n_{\perp}$) and thus propagates with a different phase velocity. At the sample output, these components are no longer in phase, $\Delta\phi \neq 0$, and one can see that their vector sum, which represents the polarisation of the total resulting field has undergone a net rotation (Figure 8B). This total field has now a component parallel to the analyzer, which can cross it and reach the detector.

The light intensity transmitted by the analyzer, i.e. the signal intensity, is:

$$I_s \propto \sin^2\left(\frac{\Delta\phi}{2}\right) \qquad (18a)$$

with the dephasing
$$\Delta\phi = \frac{\omega}{c}\left(n_\parallel - n_\perp\right)L \tag{18b}$$

L being the optical pathlength in the sample. The polarisation responsible for the signal is:

$$P_1^{(3)}(\omega_s = \omega_{pr} + \omega_{pu} - \omega_{pu}) = \varepsilon_0\left[\chi_{1221}^{(3)}E_2(\omega_{pr})E_2(\omega_{pu})E_1^*(\omega_{pu}) + \chi_{1212}^{(3)}E_2(\omega_{pr})E_1(\omega_{pu})E_2^*(\omega_{pu})\right] \tag{19}$$

where the subscript on E design the polarisation component of the field. The phase-matching condition is thus:

$$\mathbf{k_s} = \mathbf{k_{pr}} + \mathbf{k_{pu}} - \mathbf{k_{pu}} \tag{20}$$

Thus phase-matching is automatic as the signal will be 'mixed' with the transmitted probe field.

Figure 9 shows the time profile of I_s measured in toluene. The peak at $t=0$ is due to the electronic response of the solvent and the slow component reflects the molecular reorientation of toluene (nuclear response). This reorientation dynamics is complex and involves time constants of the order of 500 fs and 2-3 ps.
Such OKE profile is the time-domain equivalent of a Rayleigh wing spectrum [7].
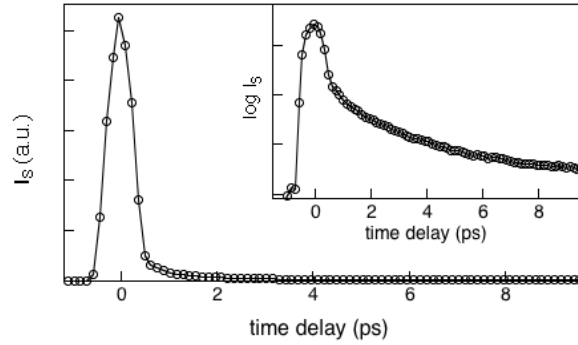
Figure 9: Transient OKE in toluene (pump at 400 nm, probe at 535 nm).

This technique is in principle very sensitivity as it has a zero-background detection scheme. However, it requires the use of a polarizer pair with a high extinction, typically 10^6 or better. If the extinction is not good, some probe light can leak through the analyzer and interfere with the signal field. In order to avoid unwanted interference with uncontrolled leaking field, one generally performs so-called optical heterodyne detection (OHD). In OHD-OKE, the signal field $\mathbf{E}_s$ is mixed with another optical field called *local oscillator* (LO), $\mathbf{E}_{LO}$ [7,8]. The detector signal is proportional to:

$$I_{OHD} \propto I_s + I_{LO} + B\left(\mathbf{E}_{LO}^*\mathbf{E}_s + \mathbf{E}_{LO}\mathbf{E}_s^*\right) = I_s + I_{LO} + 2\left(I_s I_{LO}\right)^{1/2}\cos(\Delta\phi) \tag{21}$$

where B is a constant, I_s is the intrinsic OKE intensity and is called *homodyne* signal, I_{LO} is the LO intensity, and $\Delta\phi$ is the phase difference between the signal and LO fields. The right part of eq.(21) is based on the assumption that both fields have the same polarisation. I_{LO} is constant and can be eliminated with a lock-in detection. If both fields are in phase, $\Delta\phi=0$, and if $I_{LO}\gg I_s$, the detected signal is dominated by the third term. The signal field is thus amplified upon interference with the LO field.

In OKE, the third-order polarisation oscillates at the frequency of the probe field. If the nonlinear interaction is purely non-resonant, the polarisation is entirely real, while in case of resonant interaction (see below), $\mathbf{P}^{(3)}$ contains both real and imaginary components. Both components oscillate at the same frequency but the imaginary part is $\pi/2$ out-of-phase (in quadrature) relative to the real part and to the incoming probe field. On the other hand, the field generated by the polarisation is itself $\pi/2$ phase-shifted relative to the oscillation of $\mathbf{P}^{(3)}$. As a consequence, the signal field associated with the real part of $\mathbf{P}^{(3)}$ is $\pi/2$ phase-shifted relative to the probe field, whereas the signal field associated with the imaginary part of $\mathbf{P}^{(3)}$ is in phase (emission) or π phase-shifted (absorption).

In OKE, the signal is due to a transient birefringence and is thus associated with the real part of $\mathbf{P}^{(3)}$. In OHD-OKE, the LO field has to be polarised perpendicular to the probe field (see Figure 8) and to be $\pi/2$ phase-shifted in order to interfere constructively with I_s. The LO is realized by inserting a quarter-wave plate between the crossed polarizers with the fast axis parallel to the polarisation of the probe field, that we assume to be vertical. The first polarizer is then rotated by 1 or 2°, relatively to the analyzer. This creates a horizontal component of the probe field that can go through the analyzer. Upon passing through the quarter-wave plate, this horizontal component acquires a $\pi/2$ phase shift relative to the vertical component and can now act as a LO.

If, on the other hand, one wants the LO field to enhance the resonant response of the sample, one rotates the analyzer by 1 or 2° instead of the first polarizer. This creates a horizontal component of the probe field that acts as an in-phase LO. In this case, the presence of a quarter waveplate is not necessary.

Apart from higher sensitivity, an advantage of heterodyne over homodyne detection is that the signal intensity is linear with respect to the sample response, while is it quadratic in the homodyne case.

Suppression of I_s and I_{LO} from the OHD signal can be achieved by performing one measurement with the polarizer rotated at 1 or 2° and one with the polarizer rotated at -1 or -2°. This changes the sign of $\cos(\Delta\phi)$ in eq.(21):

$$I_{OHD}^{\pm} = I_s + I_{LO} \pm 2\left(I_s I_{LO}\right)^{1/2} C \qquad\qquad (22a)$$

$$I_{OHDS} = I_{OHD}^{+} - I_{OHD}^{-} = 4\left(I_s I_{LO}\right)^{1/2} C \qquad\qquad (22b)$$

where C is a constant. The pure heterodyne signal, I_{OHDS}, is obtained by subtracting the two time profiles (eq.(22b)).

In principle, OKE is a purely non-resonant third-order process and usually performed with pump and probe pulses at the same frequency. The associated energy level scheme is shown in Figure 10A. However, optical pulses with a duration of τ_p have a frequency spectrum with a width $\Delta\nu_P = 0.441\cdot\tau_P^{-1}$ (assuming transform-limited Gaussian pulses). Thus, resonance enhancement of the nonlinear response occurs when the frequency difference of the first two interacting fields corresponds to the vibrational frequency of a Raman-active mode of the sample material (Figure 10B). In such case, the time profile of the OHD-OKE signal exhibits damped oscillations due to impulsive excitation of vibrations and the Fourier-transform is equivalent to a low-frequency Raman spectrum [9-12]. In case of resonance, $\mathbf{P}^{(3)}$ contains both real and imaginary components whose associated signal field can be measured separately by varying the phase of the LO.
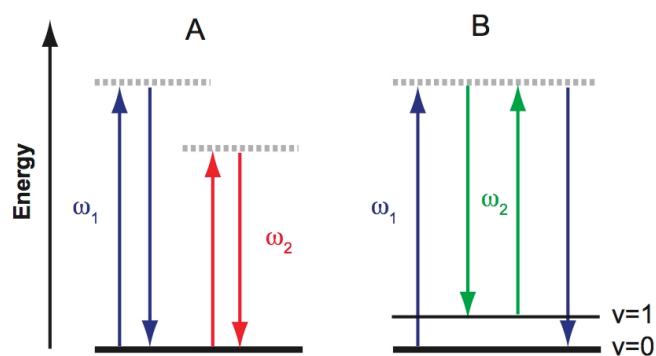
Figure 10: Energy level scheme for (A) non-resonant OKE and (B) Raman resonant OKE (RIKES).

This resonant variant is called RIKES for Raman Induced Kerr Effect Spectroscopy. When performed in the frequency domain with long ns pulses, probing is performed at a single wavelength whereas pumping is done using tunable laser pulses (or vice-versa). The OKE signal is then measured as a function of the pump-probe frequency difference and a spectrum with maxima at Raman frequencies is obtained [13].

5.2) Transient dichroism (polarisation spectroscopy)

Transient dichroism can be performed with an experimental setup very similar to that shown in Figure 7. The major difference with transient OKE is that both the pump and probe frequencies are resonant with an electronic transition of the material. Upon excitation with polarised light, the probability for a sample molecule to be excited is proportional to $\cos\Theta$, where Θ is the angle between the transition dipole moment of the molecule and the plane of polarisation of the excitation field. Thus excitation results to an orientational anisotropy of the excited molecules and of the remaining non-excited population. The lifetime of this orientational anisotropy depends on the reorientation dynamics of the molecules. A direct consequence of this anisotropy is that the absorbance of the sample depends on the polarisation of the light, i.e. the sample is dichroic. For example, let's assume that pump and probe pulses are at the same frequency and interact with the S_0-S_1 transition of the sample molecules, and let's define the following populations:

$N_\parallel^{S_0}, N_\perp^{S_0}$: number of molecules in the ground state with the transition dipole moment parallel or perpendicular to the pump field;

$N_\parallel^{S_1}, N_\perp^{S_1}$: number of molecules in the excited state with the transition dipole moment parallel or perpendicular to the pump field.

Directly after excitation, $N_\parallel^{S_1} > N_\perp^{S_1}$ and $N_\parallel^{S_0} < N_\perp^{S_0}$ and therefore light polarised parallel to excitation is less absorbed than light polarised perpendicular.

The principle of the transient dichroism is explained with Figure 11 [14]. The probe field is polarised vertically while the pump field is polarized at 45°. The electric field associated with the probe pulse can be decomposed into components parallel, $E_\parallel$, and perpendicular, $E_\perp$, to the polarisation of the pump pulse. At the entrance of the sample, these two components have the same amplitude (Figure 11A). In the dichroic sample, each component experience a different absorbance ($A_\parallel$ or $A_\perp$), the parallel component being less absorbed. At the sample output, these components have no longer the same amplitude and one can see that their vector sum, which represents the polarisation of the resulting total field, has undergone a rotation

(Figure 11B). This total field has now a component parallel to the analyzer (the signal), which can cross it and reach the detector.
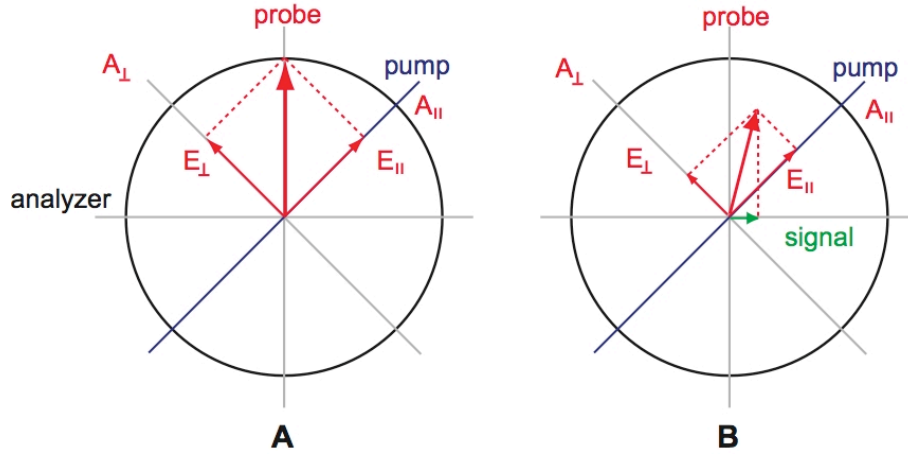
Figure 11: Principle of the transient dichroism: if there is no dichroism (**A**), both components of the probe field are absorbed similarly and the probe pulse is blocked by the analyzer. With dichroism (**B**), the two components are absorbed differently thus the polarisation of the total transmitted probe field is slightly rotated and a component parallel to the analyzer can cross it.

For heterodyne detection, the LO field has to be in phase with the probe field in order to interfere with the field generated by the imaginary (resonant) part of $\mathbf{P^{(3)}}$ but its polarisation has to be perpendicular. This is realised as explained above for OHD-OKE. Figure 12 shows the results of an OHD transient dichroism measurement performed at 400 nm with a sample solution of perylene in valeronitrile [15]. The signal intensity was measured with the analyzer rotated at +1°, I_{OHD}^+, and at -1°, I_{OHD}^-, and the pure heterodyne contribution was obtained from the difference of the two signals divided by two (see eq.22). The signal intensity at negative time corresponds to I_{LO}, and the decrease of the signal at time zero arises from the phase $\Delta\phi = \pi$ (eq.21) between the LO and the field due to the imaginary part of the nonlinear response.

The time dependence of the purely OHD signal is given by:

$$I_{OHDS}(t) \propto p(t) \cdot r(t) \propto \Delta A_{\parallel} - \Delta A_{\perp} \qquad (23)$$

where $\Delta A_{\parallel}(t)$ and $\Delta A_{\perp}(t)$ are the pump-induced absorption changes measured with probe light polarized parallel and perpendicular to the pump pulse, $p(t)$ is the time dependence of the population absorbing at the probe wavelength and $r(t)$ is that of the polarisation anisotropy. The latter is directly related to the transient dichroism:
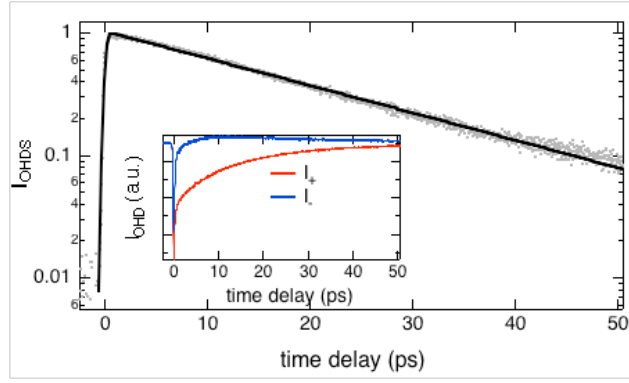
$$r(t) = \frac{\Delta A_{\parallel}(t) - \Delta A_{\perp}(t)}{\Delta A_{\parallel}(t) + 2\Delta A_{\perp}(t)} \qquad (24)$$

The amplitude of the initial polarisation anisotropy, r_0, depends on the angle γ between the transition dipole moments involved in the pumping and probing processes:

$$r_0 = \frac{3\cos\gamma - 1}{5} \qquad (25)$$

For one-photon transitions, r_0 ranges from 0.4 ($\gamma = 0°$) to -0.2 ($\gamma = 90°$).

Figure 12: Pure OHD transient dichroism signal obtained with a solution of perylene in valeronitrile (grey) and best single exponential fit (black). Inset: time profile of the signal measured with the analyzer rotated at +1° (red) and at -1° (blue).

Several processes can contribute to a temporal variation of the polarisation anisotropy: 1) molecular reorientation; 2) conversion to a different state, thus the probed transition is different and 3) excitation energy hopping. In liquid solutions, molecular reorientation is the most probable process. In this case, the decay of the polarisation anisotropy is:

$$r(t) = r_0 \exp\left(-t/\tau_{or}\right) \qquad (26)$$

where τ_{or} is the time constant of molecular reorientation. Eq.(26) is only strictly valid for spherical molecules, the reorientational dynamics of unsymmetrical rotor being in principle described by the sum of five exponential functions [8]. However eq.(26) is a good approximation in many cases. If $p(t)$ also follows an exponential dynamics with a time constant τ_{pop}, $I_{OHDS}(t)$ decays exponentially as well with a time constant:

$$\tau_{OHDS}^{-1} = \tau_{or}^{-1} + \tau_{pop}^{-1} \qquad (27)$$

Such exponential decay with a time constant of 19 ps can be observed in Figure 12. As the excited state lifetime of perylene amounts to several nanoseconds, $\tau_{OHDS}=\tau_{or}$. Thus this technique is very powerful for measuring the reorientational dynamics of molecules. Nevertheless it has the drawback that the absolute value of the polarisation anisotropy, r, is not directly accessible.

On the other hand, this technique can also be used to investigate ultrafast population dynamics, when $\tau_{pop}<<\tau_{or}$.

Finally, the signal intensity measured in OHD transient dichroism is directly related to the third-order nonlinear susceptibility:

$$I_{OHDS} \propto \text{Im}\left(\chi_{1221}^{(3)} + \chi_{1212}^{(3)}\right) \qquad (28)$$

On the other hand the homodyne signal intensity is:

$$I_{HS} \propto \left|\chi_{1221}^{(3)} + \chi_{1221}^{(3)}\right|^2 \qquad (29)$$

In this case, non-resonant contributions from the solvent may interfere with the real part of the resonant solute contribution and strongly complicating the interpretation of the signal. Thus heterodyne detection is highly recommended.

6) Basic four wave-mixing techniques

6.1) Principle
Third-order nonlinear techniques are based on the interaction of four waves. The methods described above use two beams and involve a double interaction between the material and one of the beams. Therefore they have the drawback that they do not allow the individual control (polarisation, frequency, direction) of each wave. Such control is possible with the *four-wave-mixing* techniques also called transient grating (TG) techniques [16-18]. These techniques can be explained with either the grating or the nonlinear optics formalism.
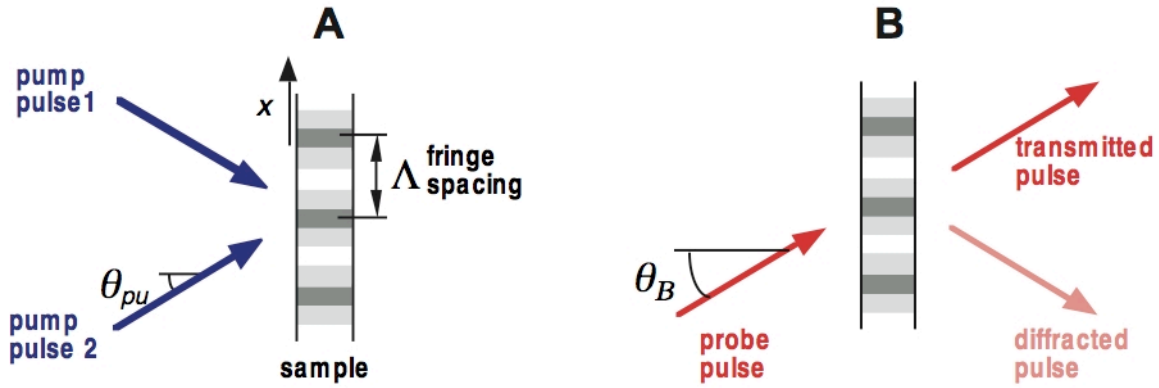
Figure 13: Principle of the TG technique.

We will start with the grating formalism, which offers a very intuitive description of the process. In the grating picture, two sequential processes can be distinguished (Figure 13):
1) Grating formation: the sample material is excited by two laser pulses at the same wavelength and crossed with an angle $2\theta_{pu}$ (Figure 13A). If the two pump pulses have the same intensity, I_{pu}, the intensity distribution in the interference region, assuming plane waves, is:

$$I(x) = 2I_{pu}\left[1 + \cos\left(\frac{2\pi x}{\Lambda}\right)\right] \qquad (30)$$

where $\Lambda = \lambda_{pu}/(2\sin\theta_{pu})$ is the fringe spacing and λ_{pu} the pump wavelength. As discussed below, there can be many types of light-matter interactions that lead to a change of the optical properties of the material. For a dielectric material, they result to a spatial modulation the optical susceptibility and thus of the complex refractive index, $\tilde{n}$. This distribution can be described as:

$$\tilde{n}(x) = \tilde{n}_0 + \Delta\tilde{n}\cos\left(\frac{2\pi x}{\Lambda}\right) \qquad (31)$$

where $\tilde{n}_0$ is the average value of the complex refractive index and $\Delta\tilde{n}$ is its light induced modulation amplitude. As shown by eqs.(3) and (4), spatial distributions of the real refractive index, n, and of the absorbance, A, with modulation amplitudes, Δn and ΔA, are also realised. Such distributions are nothing but phase and amplitude gratings, respectively.

2) Grating detection: a third laser pulse at the probe wavelength, λ_{pr}, striking this grating at Bragg angle, $\theta_B = \arcsin(\lambda_{pr}/2\Lambda)$, is partially diffracted (Figure 13B). When $\lambda_{pr} = \lambda_{pu}$, one speaks about *degenerate* TG or four-wave mixing. The diffraction efficiency, η, is given by:

$$\eta = \frac{I_s}{I_{pr}} \cong \left[\left(\frac{\ln 10 \Delta A}{4\cos\theta_B}\right)^2 + \left(\frac{\pi d \Delta n}{\lambda_{pr}\cos\theta_B}\right)^2\right] \cdot \exp\left(-\frac{\ln 10 A}{\cos\theta_B}\right) \tag{31}$$

where I_{pr} and I_s are the probe and diffracted signal intensity respectively and d is the grating thickness. This relationship is only strictly valid for small diffraction efficiency ($\eta < 0.01$).

The first and the second terms in the square bracket describe the contribution of the amplitude and phase gratings, respectively, and the exponential term accounts for the reabsorption of the diffracted beam by the sample.

The optical fields diffracted by the amplitude and phase grating are in quadrature ($\pi/2$ phase-shifted), because they originate from the imaginary and real part of the sample response. Consequently, they do not interfere and the total diffracted intensity is just the sum of the partial intensities diffracted at each grating.
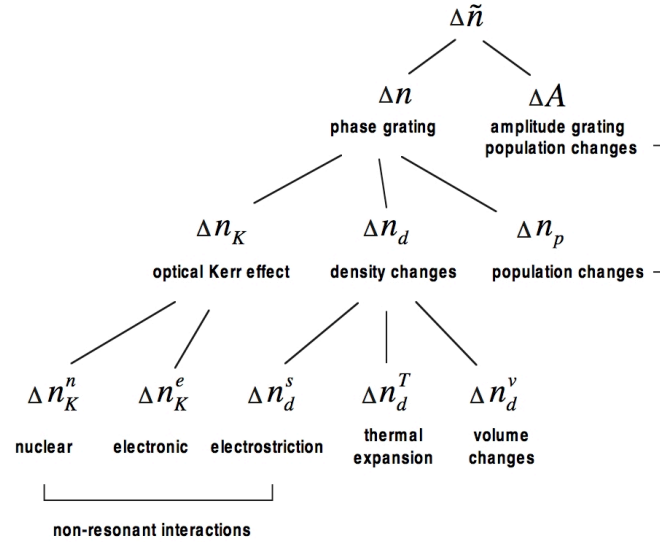
Figure 14: Classification of the contributions to a TG signal.

The main processes responsible for the variation of the optical properties of an isotropic dielectric material are summarized in Figure 14. The modulation of the absorbance, ΔA, is essentially due to the photoinduced concentration (population) change, ΔC, of the different chemical species i (excited state, photoproduct, ...):

$$\Delta A(\lambda_{pr}) = \sum_i \varepsilon_i(\lambda_{pr})\Delta C_i \tag{33}$$

where ε_i is the absorption coefficient of the species i.

The variation of the refractive index, Δn, has several origins and can be expressed as:

$$\Delta n = \Delta n_K + \Delta n_p + \Delta n_d \tag{34}$$

Δn_K is the variation of refractive index due to OKE (see section 5.1). Δn_p is the change of refractive index related to population changes. Its magnitude and wavelength dependence can be obtained by Kramers-Kronig transformation of $\Delta A(\lambda)$ or $\Delta K(\omega)$ (see eq.(5)).

Δn_d is the change of refractive index associated with density changes. Density phase gratings can have essentially three origins:

$$\Delta n_d = \Delta n_d^t + \Delta n_d^v + \Delta n_d^e \qquad (35)$$

Δn_d^t is related to the temperature-induced change of density. If a fraction of the excitation energy is converted into heat, through a non-radiative transition or an exothermic process, the temperature becomes spatially modulated. This results to a variation of density, hence to a modulation of refractive index with amplitude, Δn_d^t. Most of the temperature dependence of n originates from the density. The temperature-induced variation of n at constant density is much smaller than Δn_d^t. As discussed below, measurement of Δn_d^t can be used to do optical calorimetry [19-21].

Δn_d^v is related to the variation of volume upon population changes. This volume comprises not only the reactant and product molecules but also their environment. For example, in the case of a photodissociation, the volume of the product is larger than that of the reactant and a positive volume change can be expected. This will lead to a decrease of the density and to a negative Δn_d^v.

Δn_d^e is related to electrostriction in the sample by the electric field of the pump pulses. Like OKE, this is a non-resonant process that also contributes to the intensity dependent refractive index. Electrostriction leads to material compression in the region of high electric field strength. The periodic compression is accompanied by the generation of two counter-propagating acoustic waves with wavevectors, $\mathbf{k}_{ac} = \pm(2\pi/\Lambda)\mathbf{i}$, where $\mathbf{i}$ is the unit vector along the modulation axis. The interference of these acoustic waves leads to a temporal modulation of Δn_d^e at the acoustic frequency ν_{ac}, with $2\pi\nu_{ac}=k_{ac}v_s$, v_s being the speed of sound. As Δn_d^e oscillates between negative and positive values, the diffracted intensity, which is proportional to $\left(\Delta n_d^e\right)^2$, shows at temporal oscillation at twice the acoustic frequency [22].

In most cases, Δn_d^e is weak and can be neglected if the pump pulses are within an absorption band of the sample (resonant pumping).

The modulation amplitudes of absorbance and refractive index are not constant in time and their temporal behaviour depends on various dynamic processes in the sample. The whole point of the TG techniques is precisely the measurement of the diffracted intensity as a function of time after excitation to deduce dynamic information on the system.

In the nonlinear optics formalism, the signal is associated with the third-order nonlinear polarisation:

$$P_i^{(3)}\left(\omega_s = \omega_{pr} + \omega_{pu} - \omega_{pu}\right) = \chi_{ijkl}^{(3)}E_j\left(\omega_{pr}\right)E_k\left(\omega_{pu}\right)E_l^*\left(\omega_{pu}\right) \qquad (36)$$

Thus the phase-matching condition is the same as in eq.(20). In this case however, the two pump field interactions take place with two separate beams and phase-matching condition imposes a precise angle of incidence of the probe field. This condition is equivalent to the Bragg angle for diffraction in the grating picture. The wavevector diagram for phase matching in the case where all the beams are in the same plane of incidence is illustrated in **Figure 15**. The third-order polarisation can also be expressed in the time domain. However, the time

domain picture is not requested for understanding basic four-wave mixing experiments. This will be discussed with more complex techniques.
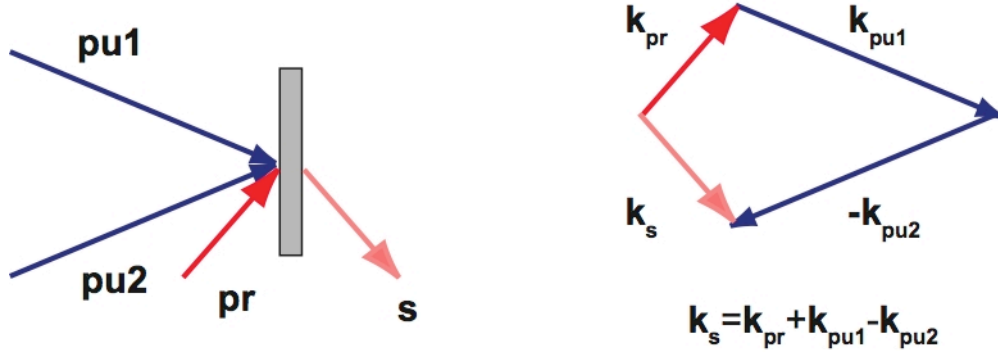
Figure 15: Transient grating beam geometry (left) and wavevector diagram (right).

As discussed above, $\chi^{(3)}$ contains 21 non-zero elements in isotropic media (see eq.(13)). In a conventional TG experiments, the two pump pulses are at the same frequency and are time coincident. Therefore, their indices can be interchanged. In this case, $\chi^{(3)}_{1212} = \chi^{(3)}_{1221}$ and the number of independent tensor elements is further reduced:

$$\chi^{(3)}_{1111} = \chi^{(3)}_{1122} + 2\chi^{(3)}_{1212} \tag{37}$$

The tensor $\chi^{(3)}$ can be factorised into four tensors according to the origin of the sample optical response: population (p) and density (d) changes, electronic (e) and nuclear (n) OKE:

$$\chi^{(3)} = \chi^{(3)}(p) + \chi^{(3)}(d) + \chi^{(3)}(e) + \chi^{(3)}(n) \tag{38}$$

Thus from Figure 14 and eq.(38), it appears that the TG technique can be used to investigate many different phenomena, such as for example OKE. This is the so-called TG-OKE technique where pump and probe pulses are at a wavelength where the sample does not absorb (non-resonant pumping and probing).

6.2) Density phase gratings: ultrafast optical calorimetry
In general, when the pump wavelength coincides an electronic transition of the sample material, but probing is done non-resonantly, signal intensity is:

$$I_s \propto \Delta n_d^2 \propto \left|\chi^{(3)}(d)\right|^2 \tag{39}$$

Indeed, the variation of absorbance, $\Delta A(\lambda_{pr})$, is zero and $\Delta n_p(\lambda_{pr})$ is negligibly small, i.e. $\chi^{(3)}(p) \approx 0$. Moreover, the signal can also contain contribution from the OKE, but the relative signal intensity due to this non-resonant process is in general small. Similarly, electrostriction will be neglected.
The time dependence of Δn_d is rather complicate and can be expressed as [20]:

$$\Delta n_d(t) = C \int_{-\infty}^{t} S(t-t') \cdot f(t')dt' \tag{40}$$

where C is a constant, which depends on the amount of heat deposited during the photoinduced process, on the volume changes and on the thermoacoustic properties of the

sample; $f(t)$ is a normalised function describing the time evolution of the temperature and/or volume change. In the simplest cases, this is an exponential function:

$$f(t) = \exp(-k_r t) \qquad (41)$$

where k_r is the rate constant of the photoinduced process. Finally, $S(t)$ can be considered as the sample response function to an instantaneous temperature and/or volume change:

$$S(t) = 1 - \cos(2\pi \nu_{ac} t) \exp(-\alpha_{ac} \nu_s t) \qquad (42)$$

where α_{ac} is the acoustic attenuation constant of the medium. Upon prompt heat release, thermal expansion occurs impulsively in the illuminated fringes of the grating. This process is accompanied by the generation of two counter-propagating acoustic waves similar to those discussed above for electrostriction. Because of the interference of these acoustic waves with the density grating, Δn_d oscillates between zero and positive values, and the diffracted signal intensity shows a temporal oscillation at the acoustic frequency and not at twice this frequency as for electrostriction [23]. Figure 16 shows the time profile of the diffracted intensity recorded at 532 nm with a solution of malachite green in methanol upon excitation at the same wavelength. Directly after optical excitation, the population of the S_1 state decay non-radiatively to the S_0 state within a few picosecond. This result to the 'prompt' release of 2.33 eV energy as heat. The damping of the oscillation is due to acoustic attenuation in methanol.
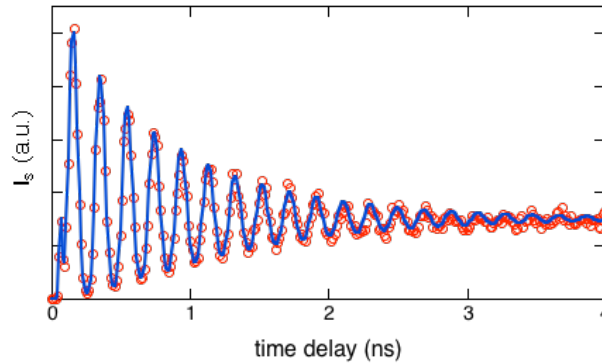
Figure 16: Time profile of the diffracted intensity measured at 532 nm with a solution of MG in methanol after excitation at the same wavelength (ν_{ac}=5.2 ns^{-1}, $k_r \approx 200$ ns^{-1}). The small initial spike is due to the contribution of ΔA to the signal.

However, if heat is not released promptly, i.e. if $k_r < \nu_{ac}$, the oscillating behaviour is less marked and vanished completely as $k_r \ll \nu_{ac}$ as illustrated in Figure 17. This figure shows that the dynamics of a heat releasing process can be recovered from the time dependence of the signal intensity. On the other hand, the amount of heat release can be deduced from the amplitude of the signal. Therefore this technique can be considered as a time-resolved optical calorimetry. Its great advantage over other optical calorimetric techniques, like the thermal lens or the photoacoustic spectroscopy is it superior time resolution. The fastest heat releasing process that can be resolved with this method is of the order of the acoustic frequency, which itself depends on the fringe spacing of the grating, Λ. The smallest Λ and thus the highest time resolution can be achieved with high crossing angle of the pump pulses. Typically a time resolution of about 100 ps can be obtained. This is at least one order of magnitude better than the other existing methods. A major difficulty of most of these techniques is the separation of the contribution from Δn_d^v and Δn_d^t to the signal, only the latter being of interest for optical

calorimetry. These two contribution can in principle be separated by performing measurements at different temperatures or in different solvents as described in detail elsewhere [20].
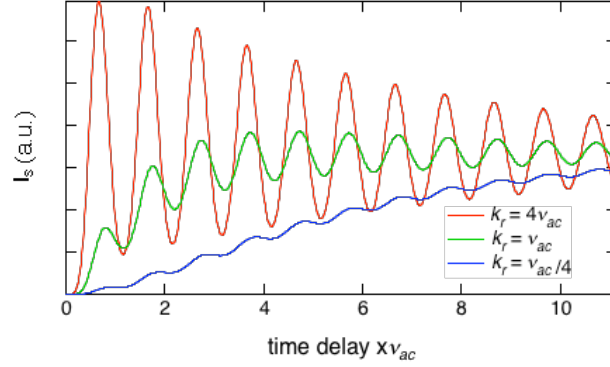
Figure 17: Time profiles of the diffracted signal intensity calculated with eq.(39) and (40)

The speed of sound in a given material can also be easily determined with this technique [22,24]. Indeed the later is given by:

$$v_s = v_{ac}\Lambda \qquad (42)$$

6.3) Measurement of population dynamics
Population dynamics can be investigated using the TG technique if the probe wavelength coincides with the absorption or dispersion spectrum of this population, i.e. by measuring $\chi^{(3)}(p)$. For this application, $\chi^{(3)}(d)$ should ideally be equal to zero. Practically, it is almost impossible to find a sample system for which a fraction of the excitation energy is not release as heat. However, the build-up of the density phase grating (Δn_d) can be slowed down when using a very small crossing angle. In such case, the acoustic frequency v_{ac} can be decreased down to 0.02 ns^{-1}. As a consequence, the signal intensity has no contribution from Δn_d during the first 10-20 ns after excitation and is given by:

$$I_s \propto \Delta A^2 + \Delta n_p^2 \propto \left|\chi^{(3)}(p)\right|^2 \qquad (43)$$

In this case, the TG technique is similar to transient absorption and allows the measurement of population dynamics. However, the sensitivity is in principle better as it is a background free technique, contrary to transient absorption where changes in the intensity of the transmitted probe pulses have to be detected. In fact, transient absorption spectroscopy is also a four-wave mixing technique where the sample undergoes a double interaction with the pump pulse electric field and a single interaction with the probe pulse electric field. Transient absorption can be considered as TG with a zero crossing angle of the pump pulses. The phase matching condition imposes that the field generated by the resulting third-order polarisation is collinear with the probe field. Therefore, the transmitted probe field acts as a LO that is in phase with the signal field generated by the imaginary part of the polarisation. Transient absorption with white light pulses could thus be called 'time-domain multiplexed two-beam heterodyne four-wave mixing spectroscopy'.
Figure 18 shows the time profile of the diffracted intensity measured with a cyanine dye in liquid solution [25]. Pump and probe pulses were at 532 nm in the S_0-S_1 absorption band of the dye. The decay of the signal reflects the recovery of the ground-state population upon relaxation from the S_1 state. The continuous line is the best fit of the convolution of the

instrument response function with an exponential function. A time constant of 210 ps is obtained. As $I_s(t) \propto \Delta C^2(t)$, the signal intensity decays twice as fast as the population. Therefore, the time constant of ground state recovery amounts to 420 ps. If the decay of the signal intensity is non-exponential, it is recommended to analyse $\sqrt{I_s(t)}$ instead of $I_s(t)$.
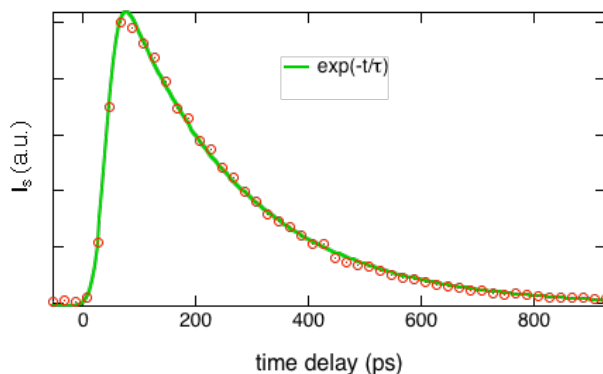
Figure 18: Time profile of the diffracted intensity recorded with a cyanine dye solution.
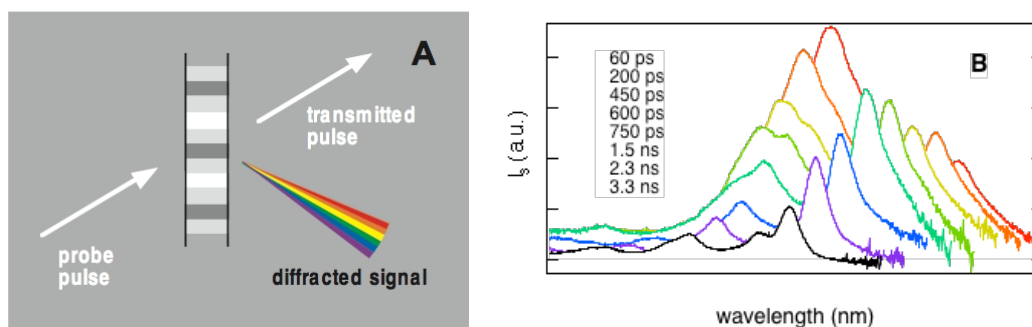
Figure 19: Principle of the multiplex TG technique (A) and TG spectra recorded at various delays after excitation of an electron acceptor in an acetonitrile solution containing an electron donor (B).

In the above example, monochromatic pulses where used for probing. In multiplex TG, the grating is probed with white light pulses generated by focusing femtosecond or picosecond pulses in a dispersive medium (self-phase modulation) [26]. If the crossing angle of the pump pulse is small enough (≤1°), the phase-matching condition is fulfilled for a wide range of probe wavelengths. As shown in Figure 19A, the different spectral components of the probe pulses are diffracted at different angles with an efficiency that depends on the wavelength dependence of ΔA and Δn_p. The so-called TG spectrum consists in the sum of the square of the transient absorption and transient dispersion spectra (eq.43). TG spectra recorded at different time delays after excitation of an electron acceptor (a cyanoanthracene derivative) in the presence of an electron donor are shown in Figure 19B [27]. At early time delays, the spectrum is due to the excited-state of the acceptor. At later time delays, these bands decay and new bands due to the acceptor radical anion appear. Such TG spectra are very similar to transient absorption spectra, the main different being that the TG intensity is always positive and thus differentiating excited state absorption and ground-state bleaching or stimulated emission can become problematic. Such multiplex TG is a valuable alternative to conventional transient absorption spectroscopy, as it is less sensitive than the latter to instability of the white light pulses [26]. However, the interpretation of the TG signal is more

difficult especially when other phenomena than population changes contribute to the signal [28].

6.4) Polarisation gratings (crossed gratings).

A so-called polarisation or crossed grating can be realised when the two pump pulses have a perpendicular linear polarisation [29]. In this case, the light intensity in the beam-crossing region is uniform, but the polarisation of the light is spatially modulated. Indeed, it varies periodically from left circular polarised (lcp) to linear polarised at +45º (p), to right circular polarised (rcp) and to linear polarised at -45º (m), and so on, as shown in Figure 20A.
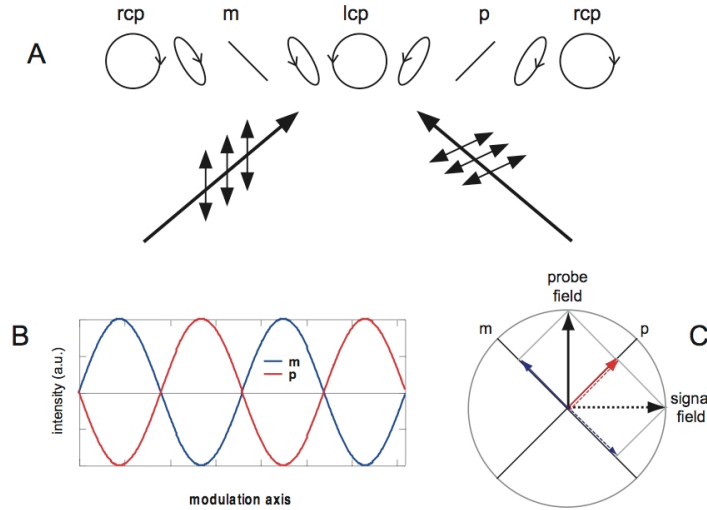
Figure 20: Principle of the polarisation grating technique: spatial dependence of the polarisation in the crossing region of two linearly but perpendicularly polarised pump pulses (A); spatial dependence of the light intensity with linear polarisation at -45° (m) and +45° (p) (B); origin of the rotation of the polarisation of the signal field relative to the probe field (C).

Such a polarisation grating, where the total light intensity is constant, can be described as the sum of four intensity gratings having each a different polarisation [30]:

$$I^{PG}(x) = I^{lcp}(x) + I^{p}(x) + I^{rcp}(x) + I^{m}(x) \tag{44}$$

If the sample molecules are not optically active, the contributions of the intensity modulation with circular polarisation cancel and only the gratings with linear polarisation are important. As shown in Figure 20B, these two intensity gratings are π out of phase. Upon interaction with the material sample, the polarisation of the intensity gratings is stored as modulations of the orientational anisotropy in the p and m directions. This can result for example to two amplitude gratings associated with molecules having their transition dipole moment along the p and m directions, respectively. As already discussed in section 5.1, the electric field associated with the linearly polarised probe beam can be decomposed into two perpendicular components polarised at ±45° (Figure 20C). Each component interacts with the corresponding grating (p or m) and is partially diffracted. As both gratings are out of phase, the diffracted components are also 180º out of phase. Consequently, the polarisation of the diffracted beam is rotated by 90º relatively to the probe beam. Experimentally, a polarizer oriented perpendicular to the polarisation of the probe light is placed in front of the detector to ensure that the measured signal is only due to the polarisation grating.

The decay of such a polarisation grating is due to both population relaxation and reorientation of the transition dipole of the molecules. The time dependence of the signal intensity is given by:

$$I_s(t) \propto \left[p(t) \cdot r(t) \right]^2 \propto \left| \chi_{1212}^{(3)} \right|^2 = \left| \chi_{1221}^{(3)} \right|^2 \qquad (45)$$

The temporal dependence of the signal intensity is essentially the same as that for transient dichroism (section 5.1, eq.(23)), the only difference being the quadratic dependence of the signal intensity, because of the homodyne detection. In terms of nonlinear optics, the polarisation grating technique probes the $\chi_{1212}^{(3)}$ or the $\chi_{1221}^{(3)}$ tensor elements. In a conventional TG experiments where both pump pulses are at the same wavelength and are time coincident, these two tensor elements are identical. As a consequence, the polarisation grating technique can be considered a four wave-mixing variant of homodyne transient dichroism. Its applications are thus the same [31,32].
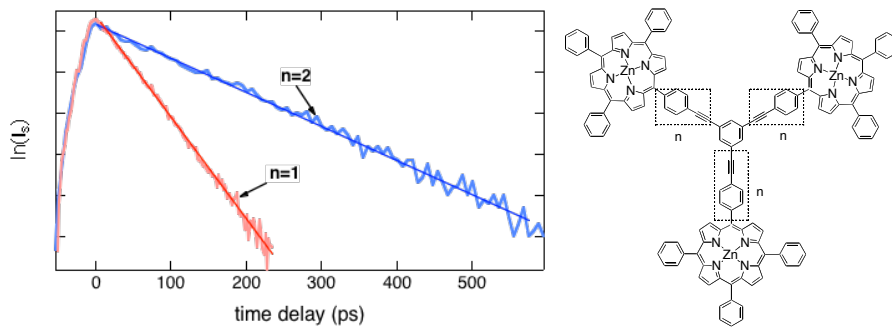
Figure 21: Time profiles of the intensity diffracted from a polarisation grating generated upon excitation at 532 nm of a solution containing triporphyrin arrays with different spacer length.

Figure 21 shows the time evolution of the intensity diffracted from a polarisation grating obtained with a solution containing a triporphyrin molecule [33]. The decay of the signal is due to the decrease of the polarisation anisotropy caused by the hopping of the excitation energy from one porphyrin unit to another.

Another interesting aspect of the polarisation grating geometry is that density phase gratings are suppresses. Indeed as excitation intensity is uniform, the concentration of the various species is not spatially modulated and heat is dissipated uniformly. This possible contribution of thermal density phase grating to the signal can be clearly ruled out.

6.5) Polarisation-selective TG

The effect of polarisation discussed in the previous section can be further used to selectively suppress one of the four contributions to $\chi^{(3)}$, namely population changes, density changes, electronic and nuclear Kerr effect (eq.(38)) [34]. Each of these contributions is associated with a tensor characterised by different symmetry properties. For example, the relationship between the four non-vanishing tensor elements related to the electronic OKE, $\chi^{(3)}(e)$, is:

$$\chi_{1111}^{(3)}(e) = 3\chi_{1122}^{(3)}(e) = 3\chi_{1212}^{(3)}(e) \qquad (46)$$

Other relationships exist for $\chi^{(3)}(n)$, $\chi^{(3)}(p)$ and $\chi^{(3)}(d)$, as summarised in Table 2.

Table 2: Relative magnitude of the tensor elements of the third-order nonlinear susceptibility originating from various processes and polarisation angle, ζ, of the signal beam, where the contribution of the corresponding process vanishes for the set of polarisation (ζ, 45°, 0, 0).

Process	$\chi_{1111}^{(3)}$	$\chi_{1122}^{(3)}$	$\chi_{1212}^{(3)}$	ζ
electronic	1	1/3	1/3	-71.6°
nuclear	1	-1/2	3/4	63.4°
density	1	0	0	-45°
population:				
$\gamma = 0°$ ($r = 0.4$)	1	1/3	1/3	-71.6°
$\gamma = 90°$ ($r = -0.2$)	1	2	-1/2	-26.6°
no correlation ($r = 0$)	1	0	0	-45°

Experimentally, each of these tensor elements can be measured by choosing the appropriate polarisation of the three incoming optical fields and of the signal field. This table also gives the angle ζ, at which the contribution vanishes with the set of polarisation (ζ, 45°, 0°, 0°). For example, if the two pump beams are vertically polarised and if the probe beam is at 45°, the signal component polarised at ζ=-45° does not contain any density contribution, $\chi_{1212}^{(3)}(d) = 0$.
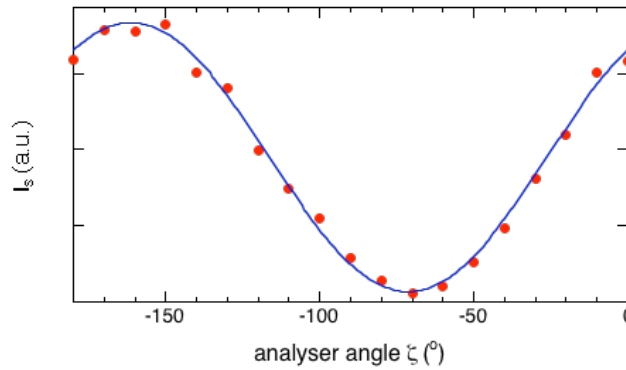
Figure 22: Dependence on the analyzer angle, ζ, of the signal intensity measured in pure acetonitrile at zero time delay.

Figure 22 shows the ζ–dependence of the signal intensity recorded in the (ζ, 45°, 0°, 0°) geometry with pure acetonitrile at zero time delay. The intensity vanishes at about -72° indicating that electronic OKE is at the origin of the signal. When pumping and probing non-resonantly, the dominant contributions to the signal are the electronic and nuclear OKE. Polarisation selective TG offers a unique opportunity to measure these two processes separately [35].
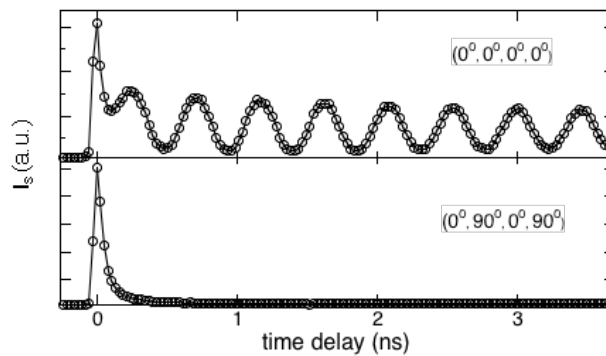
Figure 23: Time profiles of the diffracted signal intensity after 355 nm excitation of a suspension of TiO_2 particles in water using different sets of polarisation of the four beams.

Figure 23 shows the time profiles of the diffracted signal intensity measured after excitation at 355 nm of a suspension of TiO_2 particles in water. The upper profile has been measured with all four waves polarised vertically and reflects $\chi^{(3)}_{1111}$, which contains contributions from $\chi^{(3)}_{1111}(p)$ and $\chi^{(3)}_{1111}(d)$. $\chi^{(3)}_{1111}(p)$ is due to the trapped electron population that decays by charge recombination, whereas $\chi^{(3)}_{1111}(d)$ is due to the heat dissipated upon charge separation and recombination. The contributions of $\chi^{(3)}_{1111}(e)$ and $\chi^{(3)}_{1111}(n)$ can be neglected on this timescale. The time profile in the lower panel has been measured with the set of polarisation ($0°$, $90°$, $0°$, $90°$) and thus reflects $\chi^{(3)}_{1111}(p)$ only.

7) Advanced four-wave mixing techniques

In the basic four-wave mixing techniques discussed in the previous chapter, both pump pulses are time coincident and are at the same wavelength.

However, variants of these techniques where the pump pulses are at different wavelengths or are not time-coincident allow different phenomena and processes to be investigated. CARS and three-pulses photon-echo spectroscopy are such variants that we will discuss now.

7.1) Coherent Anti-Stokes Raman Scattering (CARS) spectroscopy

CARS is a nonlinear Raman spectroscopy involving the interaction of four optical fields, as illustrated in Figure 24 [13,36]. Practically, in CARS the sample is irradiated with two beams at ω_1 and ω_2. The ω_1 beam is usually called pump beam, whereas the ω_2 is the Stokes beam. If the frequency difference $\Delta\omega = \omega_1 - \omega_2$ is equal to the frequency ω_{ab} of a Raman active vibrational mode of the sample molecule, light at $\omega_{as} = \omega_1 + \omega_{ab}$ is generated and propagates in a well-defined direction determined by the phase-matching condition (see below). In a typical CARS experiment, the signal intensity at ω_{as} is recorded while ω_2 is varied and ω_1 is kept fixed.

The advantages of CARS over linear Raman spectroscopy are the following:
- the intensity of the CARS signal is much larger and the signal propagates in a well-defined direction. This results in a signal luminosity that is 10^5 - 10^{10} times larger than in linear Raman;
- Raman spectra of emitting samples (flames, fluorescing species, ...) as well as diluted samples (gases, ...) can be recorded by CARS spectroscopy.
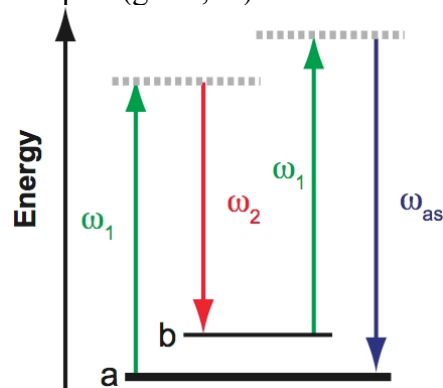
Figure 24: Energy level scheme for CARS.

CARS can also be discussed in terms of TG (Figure 25). However, contrary to the cases discussed above, the distribution of light intensity in the crossing region of two beams at different frequencies, ω_1 and ω_2, is not a stationary modulation as described by eq.(29) but is time-dependent. Indeed, the intensity at a given position in the crossing region varies

periodically with the beat frequency $\Delta\omega = \omega_1 - \omega_2$. In other words, the fringes of the interference pattern move along the modulation axis at the frequency $\Delta\omega$. Such grating is called *moving grating* [37]. If the frequency of the moving grating is equal to that of a Raman active mode of the sample molecules, the sweeping electric field drives coherently the vibrational motion of the molecule at the frequency ω_{ab}, the coupling parameter between the electric field and the molecules being $\partial\alpha/\partial q$, where α is the polarisability and q the coordinate of a vibrational normal mode. Thus all the molecules vibrate coherently along q. This coherent vibrational motion creates a temporal and spatial modulation of the refractive index at the frequency ω_{ab}. A second beam at ω_1 probing this modulation is diffracted into a well-defined direction if the Bragg condition is fulfilled and its frequency is shifted to $\omega_1 + \omega_{ab}$. This shift is due to the temporal modulation of the grating. It should be noted that probing beam does not have to be at ω_1, but it is generally the case for practical reasons.
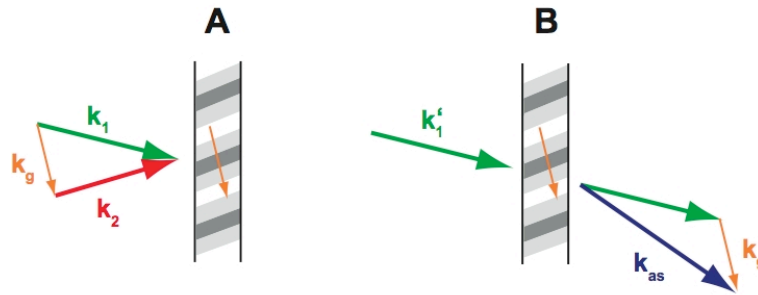

Figure 25: Grating picture of CARS spectroscopy (the tilt of the fringes is due to the motion of the grating).

The phase-matching condition is:

$$\mathbf{k}_{as} = \mathbf{k}_1' + \mathbf{k}_g = \mathbf{k}_1' + \mathbf{k}_1 - \mathbf{k}_2 \tag{47}$$

where $\mathbf{k}_g$ is the grating vector, $\mathbf{k}_g = \mathbf{k}_1 - \mathbf{k}_2$, and $\mathbf{k}_1'$ is the wavevector associated with the second beam at ω_1.

Figure 26 shows the wavevector diagrams for several CARS geometries. The collinear geometry (B) can only be applied in the gas phase, where the refractive index does almost not depend on frequency. In liquids, the other geometries have to be used.
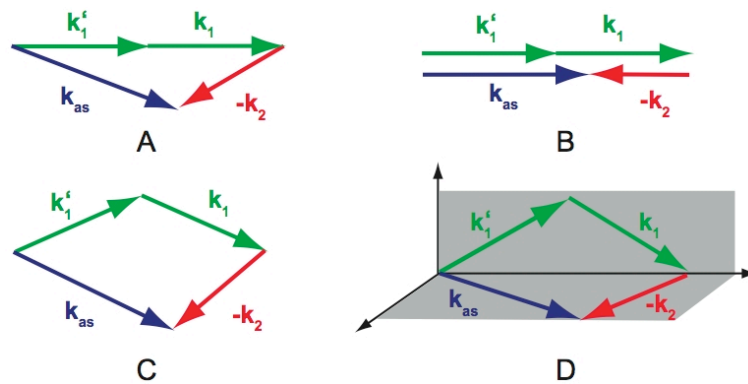
Figure 26: Phase-matching geometries for CARS: A) general case, B) collinear (gas phase only), C) in-plane four-wave mixing, D) folded boxcars.

The CARS intensity is given by eq.(15) with the corresponding tensor elements:

$$I_{CARS} \propto \left| \chi_{ijkl}^{(3)}\left(\omega_{as} = 2\omega_1 - \omega_2 \right) \right|^2 \qquad (48)$$

For a four-level systems as that shown in Figure 24, $\chi^{(3)}$ contains a very large number of terms and for simplicity one can split it into a non-resonant electronic part and a Raman resonant part, the latter being responsible for the enhancement of the signal intensity when $\Delta\omega = \omega_{ab}$:

$$\chi^{(3)} = \chi^{(3)}(NR) + \chi^{(3)}(R) \qquad (49)$$

Being non-resonant, $\chi^{(3)}(NR)$, is purely real, whereas $\chi^{(3)}(R)$ contains real and imaginary parts:

$$\chi^{(3)}(R) = \chi_r^{(3)}(R) + i\chi_i^{(3)}(R) \qquad (50)$$

Figure 27 shows the magnitude of the real and imaginary parts of $\chi^{(3)}(R)$ around ω_{ab}.
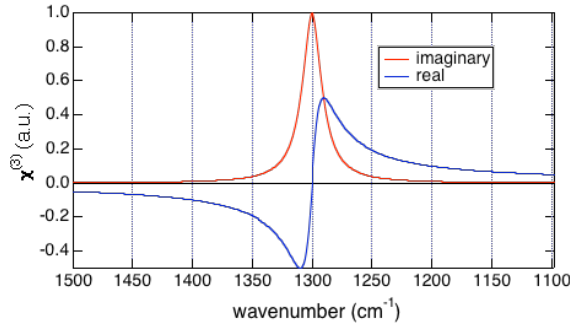
**Figure 27:** Lineshapes of the real and imaginary parts of $\chi^{(3)}(R)$

As discussed in section 6.1, the optical fields generated by the imaginary and real part of the susceptibility are in quadrature ($\pi/2$ phase-shifted) and therefore the CARS intensity is given by:

$$I_{CARS} \propto \left(\chi_{ijkl,i}^{(3)}(R) \right)^2 + \left(\chi_{ijkl,r}^{(3)}(R) + \chi_{ijkl,r}^{(3)}(NR) \right)^2 \qquad (51)$$

One can see that the real components of $\chi^{(3)}$ interfere though the cross product $2\chi_{ijkl,r}^{(3)}(R)\chi_{ijkl,r}^{(3)}(NR)$. Therefore the non-resonant contribution amplifies the real part of $\chi^{(3)}(R)$ at the expense of the imaginary part. Very intense CARS bands look Lorentzian because the first term of the r.h.s. of eq.(51) dominates, whereas weak CARS lines look dispersive because the cross product is predominant. In the gas phase, $\chi^{(3)}(NR)$ is negligibly small and the CARS lines are Lorentzian.

Figure 28 shows spectra obtained by multiplex CARS spectroscopy. The pump pulse at ω_1 was monochromatic (at 532 nm) while the Stokes pulse had a broad spectrum around 575 nm with a width of about 30 nm. The latter was realised by amplifying a portion of the spectrum of white light pulses. In CCl$_4$, the CARS spectrum is due to $\chi^{(3)}(NR)$ only. The Gaussian shape reproduces the spectrum of the Stokes beam and the phase-matching width. Indeed the angle of incidence of the beams was optimised for phase matching with the central part of the Stokes pulse spectrum. The CARS spectrum of propionitrile (PrCN) shows contribution from $\chi^{(3)}(R)$ as well. When $\chi_{ijkl,r}^{(3)}(R) \gg \chi_{ijkl,r}^{(3)}(NR)$, the bands are Lorentzian (see at 2300 cm^{-1}), whereas when $\chi_{ijkl,r}^{(3)}(R) \approx \chi_{ijkl,r}^{(3)}(NR)$, the CARS bands are dispersive (see at 1500 cm^{-1}).

Therefore, the determination of the exact vibrational frequencies can be rather difficult, and requires a detailed spectral analysis.
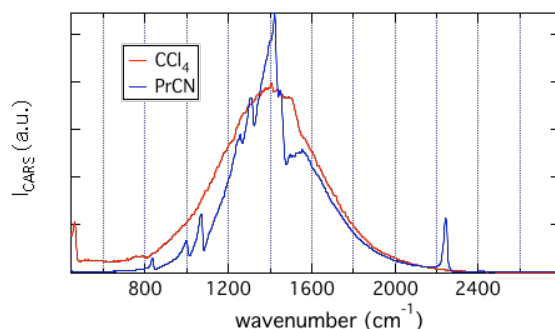
Figure 28: CARS spectra of pure solvents measured with pump pulses at 532 nm and Stokes pulses at 560-590 nm.

Further enhancement of the CARS signal is obtained when ω_1, ω_2 and/or ω_{as} correspond to the frequency of an electronic transition of the sample molecule. This is electronic-resonant CARS by analogy to resonant Raman. This resonance effect allows CARS lines of very diluted molecules to be detected. It offers also the possibility to perform time-resolved resonant CARS (TR^2-CARS) spectroscopy [38,39]. In this case, the sample is first excited by an actinic pulse, which triggers a photochemical or photophysical process. After a given time delay, a CARS measurement is performed. If the Stokes pulse is monochromatic, its frequency is tuned and the intensity of the signal is recorded as a function of ω_2.
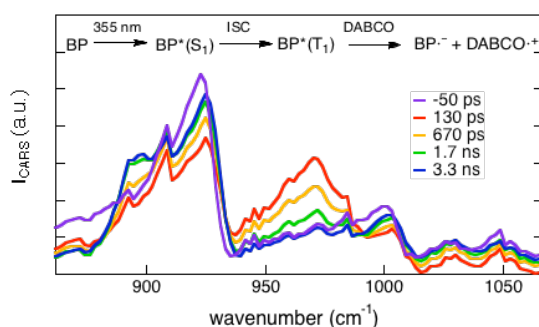
Figure 29: TR^2-CARS spectra recorded at different time delays after excitation of benzophenone (BP) in acetonitrile in the presence of DABCO.

Picosecond TR^2-CARS is performed in the multiplex mode, i.e. by using broadband Stokes pulses, by dispersing the resulting signal and recording the spectrum with a multichannel detector. For example, Figure 29 shows TR^2-CARS spectra obtained after excitation of benzophenone (BP) in the presence of diazabicyclooctane (DABCO) in acetonitrile with an actinic pulse at 355 nm. The band around 970 cm^{-1} is due to the triplet state of BP, which is very rapidly populated by intersystem crossing (ISC) from the S_1 state. The T_1-T_n transition is resonant with the CARS pump pulse at 532 nm. This band decays upon electron transfer between BP*(T_1) and DABCO and a new band around 890 nm appears. This band can be assigned to the radical anion of BP that is in preresonance with the Stokes pulse. The band at 920 cm^{-1} is a non resonant CARS line due to the solvent.

A major problem of TR^2-CARS is the saturation of the resonant bands, which takes place in the MW/cm^2 regime already. This means that, when using 10 ps pulses, energy/pulse higher than a few nJ should be avoided. Otherwise, the CARS spectrum is dominated by non

resonant lines of the solvent. With nJ pulses, the intensity of the CARS signal is of course small and therefore the experiment has to be performed at high repetition rate. Performing TR^2-CARS with sub-ps pulses is not adequate, because of the loss of spectral resolution associated with the large spectral bandwidth.

7.2) Three-pulse photon echo (TPE) spectroscopy

Photon echo has been first reported by Kurnit et al. in 1964 with Ruby at liquid He temperature, using two 100 ns-pulses generated by a Ruby laser [40]. It was found that, upon irradiation of the sample with two crossed pulses separated by a time delay Δt_{12}, the sample emits an optical signal in a well-defined direction and with a time delay Δt_{12} with respect to the second excitation pulse. This signal is the photon echo by analogy with the well-known spin echo. The intensity of the echo was found to decrease exponentially with increasing Δt_{12}:

$$I_{PE}(\Delta t_{12}) \propto \exp(-4\Delta t_{12}/T_2) \tag{52}$$

where T_2 is the electronic dephasing time of the sample molecules.

A detailed understanding of the photon echo requires a theoretical description based on the density matrix formalism and on the time-dependent perturbation theory [41,42]. This goes however beyond the scope of this lecture and we will thus limit us to a qualitative and 'intuitive' description of this phenomenon.

The photon echo signal is directly related to the third-order polarisation. In this case, it is better to express the third-order polarisation in the time domain:

$$\mathbf{P}^{(3)}(t) = \int_0^\infty dt_3 \int_0^\infty dt_2 \int_0^\infty dt_1 \mathbf{R}(t_3,t_2,t_1)\mathbf{E}(t-t_3)\mathbf{E}(t-t_3-t_2)\mathbf{E}(t-t_3-t_2-t_1) \tag{53}$$

where $\mathbf{R}$ is the sample 3rd order nonlinear response function and is related to the Fourier transform of the third-order nonlinear susceptibility $\chi^{(3)}$. $\mathbf{R}$ can be expressed as the sum of 48 terms, which correspond to all possible contributions of three incoming fields to the polarisation. Each of these terms can be associated with a distinct time evolution of the density matrix i.e. with a distinct Liouville pathway [41]. They correspond to different phenomena and can be sometimes measured separately because of different phase-matching conditions or different pulse sequences.
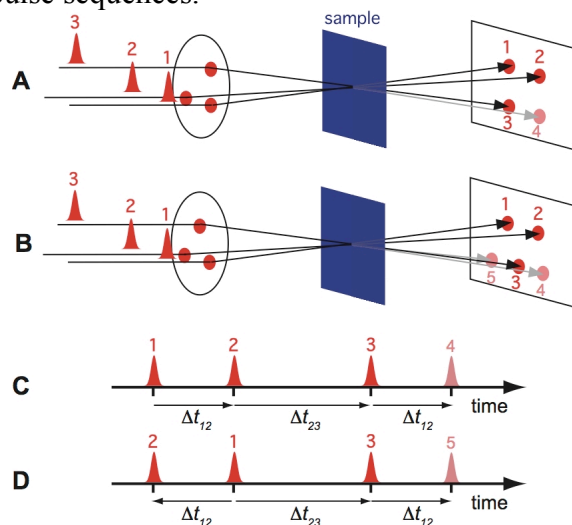
Figure 30: Geometries for TPE (A, B) and pulse sequences (C, D).

In the original photon echo experiment, only two optical pulses were used. However, in this two-pulse photon echo, the sample molecules interact twice with the second pulse. In order to have a better control of the experiment, one usually prefers the three-pulse photo echo (TPE) technique, also called stimulated photon echo, where the echo originates from a single interaction with each of the three incoming pulses . Typical experimental geometries for TPE are depicted in Figure 30. In **A**, a conventional TG experiment is realised if Δt_{12}=0 and if the signal intensity is recorded as a function of Δt_{23}, the population period. To observe a photon echo signal in the phase-matching direction $\mathbf{k_s}=\mathbf{k_3}+\mathbf{k_2}-\mathbf{k_1}$ (position 4), pulse 1 must strike the sample before pulse 2, i.e. Δt_{12}>0 (sequence C). On the other hand, the observation of a photon echo when Δt_{12}<0 (sequence D) requires a different beam geometry as the phase-matching condition is $\mathbf{k_s}=\mathbf{k_3}-\mathbf{k_2}+\mathbf{k_1}$. When the sample thickness is small enough, $d \approx \Lambda$, the phase-matching condition is partially alleviated and 'thin grating' regime prevails. This means that a diffracted signal is observed even if the angle of incidence of the probe beam departs from the Bragg angle. In terms of nonlinear optics, this is equivalent to the case where the sample thickness, d, is smaller than the critical length, L_c= 2/Δk (see eq.(10)). In this case, geometry B can be used. Its advantage is that both echo signals at Δt_{12} > 0 (position 4) and Δt_{12} < 0 (position 5) can be observed.
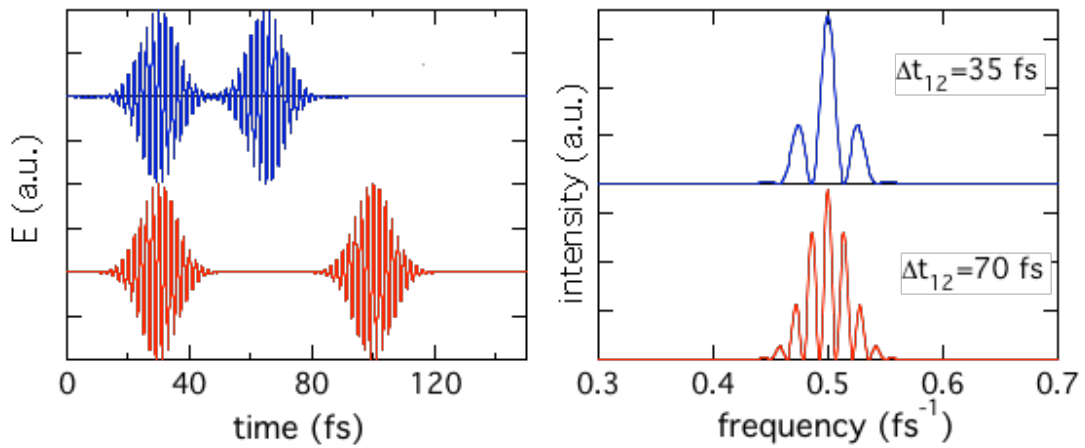
Figure 31: Electric field (left) and spectral intensity (right) associated with two 10 fs pulses separated by 35 and 70 fs.

In order to understand the origin of a photon echo, one has first to consider Figure 31, which shows the Fourier transform of the electric field associated with two optical pulses separated in time by Δt_{12}. The spectrum associated with a single transform-limited Gaussian pulse is Gaussian as well with a full width at half-maximum (fwhm) of:

$$\Delta \upsilon_P = \frac{2 \ln 2}{\pi \tau_P} \qquad (54)$$

However, the intensity spectrum associated with two such pulses separated by Δt_{12} is modulated, i.e. shows spectral fringes. The modulation increases (the spectral fringe spacing decreases) as Δt_{12} increases. This phenomenon is used in spectral interferometry to characterise the electric field of ultrashort pulses.

The second point to consider is that a photon echo is only observed if the absorption band associated with the optical transition investigated is inhomogeneously broadened. This means that all the sample molecules do not have exactly the same transition energy because for

example of slightly different environments. Thus, the absorption band of the ensemble consists in a superposition of the spectra of individual molecules and is much broader. For example, at liquid He temperature, the 0-0 absorption band of an organic dye like cresyl violet in an amorphous matrix is inhomogeneously broadened with a width of about 600 cm^{-1}. On the other hand, the absorption band of a single molecule, i.e. the homogeneous band, is Lorentzian with a width of a fraction of cm^{-1}, typically 1 GHz (1 cm^{-1}=30 GHz) [43]. The distinction between homogeneous and inhomogeneous widths is schematically depicted in Figure 32.
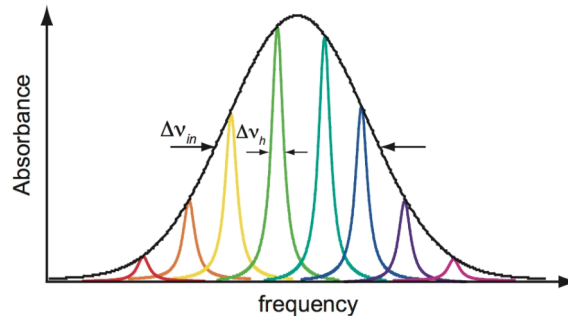
Figure 32: Homogeneous and inhomogeneous bandwidths.

Irradiation of such a inhomogeneously broadened band with two time delayed optical pulses, P1 and P2, leads to a selective excitation of subpopulations of the sample molecules with a homogeneous absorption band coinciding with the intensity spectrum of the pulse pair. The absorption spectrum just after excitation exhibits 'holes' because of these subpopulations, which have been removed from the ground state (Figure 33A). This phenomenon is commonly called *spectral hole burning* [44]. Now the sample can be considered as an optical filter, which transmits only wavelengths corresponding to the pulse pair spectrum. If one illuminates this 'filter' with a single optical pulse having a Gaussian spectrum, P3, one obtains a transmitted spectrum similar to that of the initial pulse pair (Figure 33B). Thus, the transmitted electric field is similar to that of two Gaussian pulses separated by Δt_{12}.
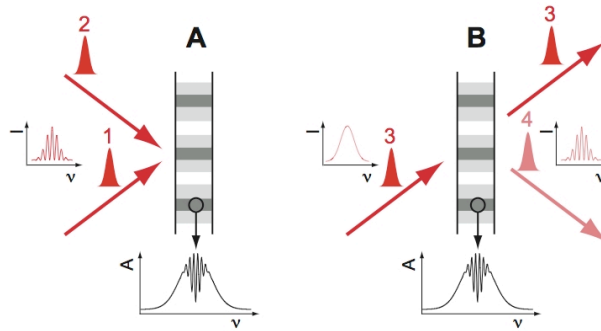
Figure 33: Transient grating description of the three-pulse photon echo technique.

Finally as the P1 and P2 are not collinear but are crossed on the sample, a spatial grating is generated additionally to the spectral grating. Thus, upon illumination of this double grating with a third pulse, P3, the resulting pulses are not collinear but have the same direction of propagation than pulses P1 and P2, as illustrated in Figure 33B.

The dependence of the echo intensity on Δt_{12} described by eq.(52) can be understood by considering that the homogeneous linewidth is:

$$\Delta \upsilon_h = \frac{1}{\pi T_2} \qquad (55)$$

Therefore, if the spacing of the spectral fringes associated with the pulse pair, P1+P2, is narrower than Δv_h, selective excitation of different subpopulations is no longer possible. In such case, the spectral modulation of the pulse pair cannot be recorded as spectral holes in the sample and no photon echo is emitted upon illumination with P3. Consequently, an echo is only generated if Δt_{12} is sufficiently small for the spectral fringes to be larger than Δv_h. This is the case when Δt_{12} is smaller than T_2.

The echo intensity depends of course also on the time delay between P2 and P3, Δt_{23}. An echo is present as long as Δt_{23} is shorter than the lifetime of the spectral holes in the sample. This time ranges from a few nanosecond, i.e. the excited-state lifetime of the molecules to several hours or longer if irradiation is accompanied by a permanent photochemical transformation.

Similarly, if the absorption band of the sample is not inhomogeneously broadened, the spectral modulation of the pulse cannot be stored. In this case, emission of a photon echo is not possible. In such case, a diffracted signal can still be measured even if P1 and P2 are not time coincident. However, this signal is not delayed by Δt_{12} relative to the transmitted P3 pulse but is time-coincident. According to the Bloch model, if one performs such experiment with sufficiently short pulses, one can see that the intensity of the diffracted signal decays exponentially:

$$I_{FID}(t) = I_{FID,0} \exp(-2t/T_2) \qquad (56)$$

This is the so-called *free induction decay* (FID).

The magnitude of T_2 depends strongly on temperature. At liquid He temperature, it is typically of the same order of magnitude as the excited-state lifetime of the sample molecules while in liquids at room temperature it is as short as a few femtoseconds to a few tens of femtoseconds.

Thus at liquid He temperature, T_2 is sufficiently large to allow the time evolution of the signal intensity to be measured. In this case, it is very easy to distinguish a photon echo and a FID.

At room temperature where T_2 is much shorter, one generally measures the time-integrated signal, $I_{int} = \int_{-\infty}^{\infty} I_S(t)dt$. For FID, the integrated signal decays exponentially with Δt_{12} as:

$$I_{int}^{FID}(\Delta t_{12}) \propto \exp(-2\Delta t_{12}/T_2) \qquad (57)$$

This dependence can be understood as follows. If P1 and P2 are not time coincident, a transient grating can be stored in the sample material only if the sample has kept a memory of the electric field of P1 when P2 arrives. The P1 field is stored in the material as a coherence between ground and excited states that can be described as a superposition of ground and excited state wavefunctions. The lifetime of this coherence is T_2. Thus if $\Delta t_{12} > T_2$, the sample has totally lost the memory of the P1 field when P2 arrives. No grating is generated and therefore no signal is diffracted.

In the case of a photon echo, I_{int}^{PE} increases slightly at very small Δt_{12} and then decays exponentially as in eq.(52):

$$I_{int}^{PE}(\Delta t_{12}) \propto \exp(-4\Delta t_{12}/T_2) \qquad (58)$$

The initial increase of I_{int}^{PE} is due to the principle of causality. Indeed, the echo cannot appear before the arrival of P3. Thus at $\Delta t_{12}=0$, only half of the echo is emitted. At larger Δt_{12} and

before dephasing is effective, the whole echo profile is present and thus I_{int}^{PE} is larger. The faster decay of I_{int}^{PE} compared to I_{int}^{FID} is due to the fact that dephasing takes place not only between P1 and P2 but also between P3 and the appearance of the echo. Two Δt_{12} dephasing periods are thus involved.

In the liquid phase at room temperature, the distinction between homogeneous and inhomogeneous broadening is not clear and depends on the timescale considered. Therefore, when performing pump-probe photon echo measurements, one does not really know whether one measures $I_{int}^{PE}(\Delta t_{12})$ or $I_{int}^{FID}(\Delta t_{12})$!

In order to have full information on the broadening mechanism, several more sophisticated photon echo techniques have been implemented [45-47]. For example, in the time-gated photon echo technique, the time evolution of the intensity of the light emitted after P3 is measured.

Alternatively, information on the echo-like or FID-like nature of the signal can be obtained more easily with the *three-pulse photon echo peak shift* (3PEPS) technique [48,49]. As discussed above the maximum of $I_{int}^{FID}(\Delta t_{12})$ occurs at $\Delta t_{12}=0$, whereas the peak value of $I_{int}^{PE}(\Delta t_{12})$ is shifted to $\Delta t_{12}>0$. In the 3PEPS technique, this peak shift is measured as a function of Δt_{23} (see Figure 34).
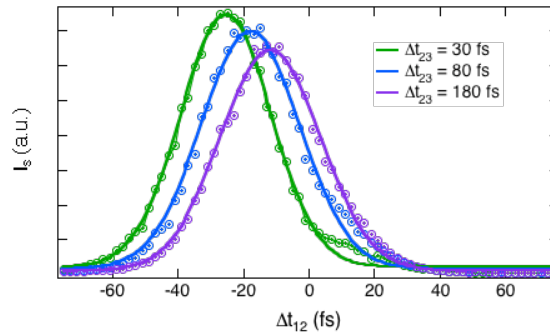

Figure 34: Δt_{12} dependence of signal intensity recorded in position 5 for different population periods, Δt_{23}, measured with an ethanol solution of IR140.

The time profile of the peak shift reflects the transition between inhomogeneous and homogeneous broadening, i.e. reflects the timescales of environment fluctuations. Let's take a polar dye dissolved in a polar solvent. When considered at very short timescale, solvent motion is frozen and each dye is surrounded by a different configuration of solvent molecules. Thus each molecule has a different transition energy and the absorption band of the ensemble is inhomogeneously broadened. On the other hand, on a long timescale, a dye molecule has experienced all possible solvent configurations. Therefore, all dye molecules have the same absorption spectrum, which is thus homogeneously broadened. Consequently, at Δt_{23} shorter than solvent motion, the spectrum is inhomogeneous and a photon echo signal is expected. In a 3PEPS measurement, a peak shift is observed. At Δt_{23} longer than solvent motion, the spectrum is homogeneous and a FID signal is expected. In a PEPS experiment, no peak shift is observed. The time evolution of the peak shift reflects thus solvent (environment) dynamics.

A 3PEPS experiment is performed as follows: for each value of Δt_{23}, Δt_{12} is scanned from negative to positive values and the signal is recorded in both positions 4 and 5 (Figure 34). In liquids, both time profiles are close to Gauss functions. If some homogeneous broadening is present, the signal at position 4 peaks at $\Delta t_{12} = \tau_{ps} > 0$, while the signal at position 5 peaks at -

τ_{ps}. If no inhomogeneous broadening is present, both signals peaks at $\Delta t_{12} = 0$. The peak shift is calculated as the time interval between the two maxima divided by 2. Figure 35 shows the time profile of the echo peak shift measured with a solution of the dye IR140 in ethanol. The oscillation of the signal is to due the propagation of a vibrational wavepacket [50].
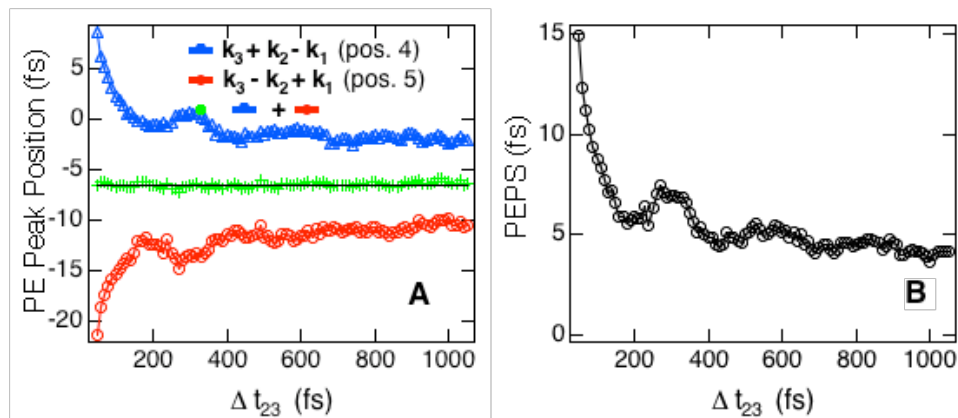
Figure 35: Peak position of the signal intensity recorded in the 4 and 5 position (A) and PEPS (B) measured with an ethanol solution of IR140.

8. Concluding remarks

We have discussed here the most used techniques based on the second and the third order nonlinear susceptibility. However over the past few years new sophisticated variants of these methods have been implemented. For example, two dimensional IR spectroscopy which has been shown to be the optical equivalent of the well-known COSY in NMR is now quite well developed [51,52]. These techniques need to be performed with ultrashort pulses on a timescale comparable or shorter that that of dephasing (T_2). These 2D spectroscopies are essentially third order nonlinear techniques where the signal basically is recorded as a function of the pump wavelength and is spectrally resolved. 2D-IR spectroscopy offers promising perspective for the elucidation of the structural dynamics of small proteins. Similarly, 2D spectroscopy in the visible region has been used to elucidate the fine details of energy migration in natural multichromophoric systems [53].

Finally, it should be noted that nonlinear optical spectroscopy is not limited to the third order susceptibility and that experimental methods based on higher orders of the susceptibility have been demonstrated. For example, the Raman echo technique, which is a fifth order method and hence involved the mixing of six waves, has been used to investigate the dynamics of liquids [54-56]. These techniques are rather complex, not only on the experimental point of view but also on the interpretation of the results as many processes can contribute to the signal [57]. Therefore, their description goes far beyond the scope of this lecture.

9. List of symbols and abbreviations

A	absorbance
ΔA	modulation amplitude of *A*
ΔC	concentration change
E	electric field

E_j	j-component of $\mathbf{E}$
E_0	electric field amplitude
f_{ijk}	nonlinear Fresnel factor
I	intensity
$\mathbf{k}$	wavevector
Δk	wavevector mismatch
k_r	reaction rate constant
K	attenuation constant
L	optical pathlength
L_c	critical length
n	refractive index
Δn_d^s	modulation amplitude of n due to electrostriction
Δn_d^T	modulation amplitude of n due to thermal expansion
Δn_d^v	modulation amplitude of n due to volume changes
Δn_K^e	modulation amplitude of n due to the electronic OKE
Δn_K^n	modulation amplitude of n due to the nuclear OKE
N	number of molecules/volume
n_0	linear refractive index
$\tilde{\mathbf{n}}$	complex refractive index
$\Delta\tilde{n}$	modulation amplitude of the complex refractive index
$\bar{n}_2$	second order nonlinear refractive index
$p(t)$	time dependence of population
$\mathbf{P}$	polarisation
$\mathbf{P^L}$	linear polarisation
$\mathbf{P^{NL}}$	nonlinear polarisation
$P_i^{(n)}$	i-component of the nth-order nonlinear polarisation $\mathbf{P^{(n)}}$
q	coordinate of a vibrational normal mode
r	polarisation anisotropy
$\mathbf{R}$	third-order nonlinear response function
r_0	initial polarisation anisotropy
t	time
Δt	time delay
T_2	dephasing time
v_s	speed of sound
α_{ac}	acoustic attenuation constant
γ	angle between transition dipole moment involved in pumping and probing
ε_0	vacuum permittivity
ε_i	molar decadic absorption coeffiction of species i
ζ	magic angle in polarisation selective TG
η	diffraction efficiency
Θ	angle between the plane of polarisation of the light and the transition dipole moment
θ	angle of incidence
θ_B	Bragg angle
λ	wavelength
Λ	fringe spacing
$\boldsymbol{\mu_{ba}}$	dipole moment for the transition from state a to state b

μ_0	vacuum permeability
ν_{ac}	acoustic frequency
$\Delta\nu_h$	homogeneous width
$\Delta\nu_{in}$	inhomogeneous width
$\Delta\nu_P$	spectral width of an optical pulse (fwhm)
τ	time constant
τ_P	pulse duration (fwhm)
$\Delta\phi$	phase difference
χ	optical susceptibility
$\chi^{(1)}$	linear optical susceptibility
$\chi^{(n)}$	nth-order nonlinear optical susceptibility
$\chi_{ijk}^{(2)}$	tensor element of $\chi^{(2)}$
$\chi_{ijkl}^{(3)}$	tensor element of $\chi^{(3)}$
ω	angular frequency
3PEPS	three-pulse photon echo peak shift
BP	benzophenone
CARS	coherent anti-Stokes Raman scattering
DABCO	diazabicyclooctane
COSY	coherent spectroscopy
DFM	difference-frequency mixing
FID	free induction decay
g	gerade
lcp	left circular polarised
LO	local oscillator
MG	malachite green
NR	non-resonant
pop	population
pr	probe
pu	pump
OHD	optical heterodyne detection
OHDS	pure heteridyne signal
OKE	optical Kerr effect
OR	optical rectification
PE	photon echo
R	resonant
rcp	right circular polarised
RIKES	Raman induced Kerr effect spectroscopy
or	diffusional reorientation
s	signal
SFG	sum-frequency generation
SHG	second-harmonic generation
TG	transient grating
TPE	three-pulse photon echo
TR^2	time-resolved resonant
u	ungerade
∥,⊥	parallel, perpendicular to the polarisation of the pump field

10. References

[1]   R.W. Boyd, Nonlinear Optics, Academic Press, Boston, 1992.

[2]   Y.R. Shen, The Principles of Nonlinear Spectroscopy, J. Wiley, New York, 2003.

[3]   K.B. Eisenthal, Acc. Chem. Res. 26 (1993) 636-43.

[4]   K.B. Eisenthal, Chem. Rev. 96 (1996) 1343-60.

[5]   G.L. Richmond, Chem. Rev. 102 (2002) 2693.

[6]   P.J. Campagnola, H.A. Clark, W.A. Mohler, A. Lewis, L.M. Loew, J. Biomed. Opt. 6 (2001) 277-86.

[7]   D. McMorrow, W.T. Lotshaw, J. Phys. Chem. 95 (1991) 10395-406.

[8]   G.R. Fleming, Chemical Applications of Ultrafast Spectroscopy, Oxford University Press, New York, 1986.

[9]   K.A. Nelson, E.P. Ippen, Adv. Chem. Phys. 75 (1989) 1.

[10]   P. Vöhringer, N.F. Scherer, J. Phys. Chem. 99 (1995) 2684.

[11]   P. Cong, H.P. Deuel, J.D. Simon, Chem. Phys. Lett. 240 (1995) 72.

[12]   G. Giraud, J. Karolin, K. Wynne, Biophys. J. 85 (2003) 1903-13.

[13]   M.D. Levenson, S.S. Kano, Introduction to Nonlinear Laser Spectroscopy, Academic Press, Boston, 1988.

[14]   D. Waldeck, A.J. Cross, D.B. McDonald, G.R. Fleming, J. Chem. Phys. 74 (1981) 3381.

[15]   A. Morandeira, A. Fürstenberg, J.-C. Gumy, E. Vauthey, J. Phys. Chem. A 107 (2003) 5375-83.

[16]   H.J. Eichler, P. Günter, D.W. Pohl, Laser-Induced Dynamic Gratings, Springer Verlag, Berlin, 1986.

[17]   J.T. Fourkas, M.D. Fayer, Acc. Chem. Res. 25 (1992) 227.

[18]   E. Vauthey, in: R.D. Guenther, D.G. Steel, L. Bayvel (Eds.), Encyclopedia of Modern Optics. Elsevier, Oxford, 2004, p. 73.

[19]   E. Vauthey, A. Henseler, J. Phys. Chem. 99 (1995) 8652.

[20]   M. Terazima, Adv. Photochem. 24 (1998) 255.

[21]   P. Brodard, E. Vauthey, Chem. Phys. Lett. 309 (1999) 198.

[22]   R.J.D. Miller, R. Casalegno, K.A. Nelson, M.D. Fayer, Chem. Phys. 72 (1982) 371.

[23]   K.A. Nelson, D.R. Lutz, M.D. Fayer, L. Madison, Phys. Rev. B 24 (1981) 3261.

[24]   P. Brodard, E. Vauthey, J. Phys. Chem. B 109 (2005) 4668.

[25]   E. Vauthey, Chem. Phys. 196 (1995) 569-82.

[26]   C. Högemann, M. Pauchard, E. Vauthey, Rev. Sci. Instrum. 67 (1996) 3449.

[27]   E. Vauthey, C. Högemann, X. Allonas, J. Phys. Chem. A 102 (1998) 7362.

[28]   E. Vauthey, J. Phys. Chem. A 105 (2001) 340.

[29]   G. Eyring, M.D. Fayer, J. Chem. Phys. 81 (1984) 4314.

[30]   J.T. Fourkas, R. Trebino, M.D. Fayer, J. Chem. Phys. 97 (1992) 69.

[31]   J.-C. Gumy, E. Vauthey, J. Phys. Chem. 100 (1996) 8628.

[32]   J.C. Gumy, O. Nicolet, E. Vauthey, J. Phys. Chem. A 103 (1999) 10737-43.

[33]   P. Brodard, S. Matzinger, E. Vauthey, O. Mongin, C. Papamicaël, A. Gossauer, J. Phys. Chem. A 103 (1999) 5858.

[34]   F.W. Deeg, M.D. Fayer, J. Chem. Phys. 91 (1989) 2269.

[35]   J. Etchepare, G. Grillon, J.P. Chambaret, G. Hamoniaux, A. Orzag, Opt. Commun. 63 (1987) 329.

[36]   H. Abramczyk, Introduction to Laser Spectroscopy, Elsevier, Amsterdam, 2005.

[37]   A.E. Siegman, Appl. Phys. Lett. 30 (1977) 21.

[38]   G.H. Atkinson, T.L. Brack, D. Blanchard, G. Rumbles, Chem. Phys. 131 (1989) 1.

[39]   J. Oberle, E. Abraham, A. Ivanov, G. Jonusauskas, C. Rulliere, J. Phys. Chem. 100 (1996) 10179.

[40]   N.A. Kurnit, I.D. Abella, S.R. Hartmann, Phys. Rev. Lett. 19 (1964) 567.

[41]   S. Mukamel, Principles of Nonlinear Optical Spectroscopy, Oxford University Press, Oxford, 1995.

[42]   W.W. Parson, Modern Optical Spectroscopy, Springer, Berlin, 2007.

[43]   E. Vauthey, K. Holliday, C. Wei, A. Renn, U.P. Wild, Chem. Phys. 171 (1993) 253.

[44]   W.E. Moerner, Persistent Spectral Hole-Burning:Science and Applications, Springer-Verlag, Berlin, 1988.

[45]   K. Duppen, F.d. Haan, E.T.J. Nibbering, D.A. Wiersma, Phys. Rev. A 47 (1993) 5120.

[46]   W.P. de Boeij, M.S. Pshenichnikov, D.A. Wiersma, Chem. Phys. Lett. 238 (1995) 1.

[47]   W.P. de Boeij, M.S. Pshenichnikov, D.A. Wiersma, Annu. Rev. Phys. Chem. 49 (1998) 99.

[48]   G.R. Fleming, M. Cho, Annu. Rev. Phys. Chem. 47 (1996) 109.

[49]   S.A. Passino, Y. Nagasawa, T. Joo, G.R. Fleming, J. Phys. Chem. 101 (1997) 725.

[50]   B. Lang, G. Angulo, E. Vauthey, J. Phys. Chem. A 110 (2006) 7028.

[51]   N.-H. Ge, R.M. Hochstrasser, PhysChemComm 3 (2002) b109935c.

[52]   J. Bredenbeck, J. Helbing, P. Hamm, J. Chem. Phys. 121 (2004) 5943.

[53]   M. Cho, H.M. Vaswani, T. Brixner, J. Stenger, G.R. Fleming, J. Phys. Chem. B 109 (2005) 10542.

[54]   M. Cho, G.R. Fleming, J. Phys. Chem. 98 (1994) 3478.

[55]   K. Tominaga, K. Yoshihara, Phys. Rev. Lett. 74 (1995) 3061.

[56]   A. Tokmakoff, M.J. Lang, D.S. Larsen, G.R. Fleming, Chem. Phys. Lett. 272 (1997) 48.

[57]   D.A. Blank, L.J. Kaufman, G.R. Fleming, J. Chem. Phys. 111 (1999) 3105.